Monthly Notices
of the
ROYAL ASTRONOMICAL SOCIETY

MNRAS **485,** 4641–4657 (2019)
Advance Access publication 2019 March 14

doi:10.1093/mnras/stz728

Mixing by overshooting and rotation in intermediate-mass stars

Guglielmo Costa [1,2★] Léo Girardi,[3] Alessandro Bressan,[1,2] Paola Marigo,[4] Thaíse S. Rodrigues [3] Yang Chen [4] Antonio Lanza[1] and Paul Goudfrooij[5]

[1]*SISSA, via Bonomea 365, I-34136 Trieste, Italy*
[2]*IFPU - Institute for Fundamental Physics of the Universe, Via Beirut 2, 34014, Trieste, Italy*
[3]*Osservatorio Astronomico di Padova – INAF, Vicolo dell'Osservatorio 5, I-35122 Padova, Italy*
[4]*Dipartimento di Fisica e Astronomia Galileo Galilei, Università di Padova, Vicolo dell'Osservatorio 3, I-35122 Padova, Italy*
[5]*Space Telescope Science Institute, 3700 San Martin Drive, Baltimore, MD 21218, USA*

Accepted 2019 March 7. Received 2019 March 7; in original form 2018 November 9

ABSTRACT

Double-line eclipsing binaries (DLEBs) have been recently used to constrain the amount of central mixing as a function of stellar mass, with contrasting results. In this work, we reanalyse the DLEB sample by Claret & Torres, using a Bayesian method and new PARSEC tracks that account for both convective core overshooting and rotational mixing. Using overshooting alone, we obtain that, for masses larger than about 1.9 $M_\odot$, the distribution of the overshooting parameter, λ_{ov}, has a wide dispersion between 0.3 and 0.8, with essentially no values below $\lambda_{ov} = 0.3$ and 0.4. While the lower limit supports a mild convective overshooting efficiency, the large dispersion derived is difficult to explain in the framework of current models of that process, which leave little room for large randomness. We suggest that a simple interpretation of our results can be rotational mixing: Different initial rotational velocities, in addition to a fixed amount of overshooting, could reproduce the high dispersion derived for intermediate-mass stars. After a reanalysis of the data, we find good agreement with models computed with a fixed overshooting parameter, $\lambda_{ov} = 0.4$, and initial rotational rates, ω, uniformly distributed in a wide range between 0 and 0.8 times the break-up value, at varying initial mass. We also find that our best-fitting models for the components of α Aurigae and TZ Fornacis agree with their observed rotational velocities, thus providing independent support to our hypothesis. We conclude that a constant efficiency of overshooting in concurrence with a star-to-star variation in the rotational mixing might be crucial in the interpretation of such data.

Key words: convection – binaries: eclipsing – stars: evolution – stars: fundamental parameters – stars: interiors – stars: rotation.

1 INTRODUCTION

Convection is one of the most uncertain processes in stars. In the context of 1D models of stellar evolution, the most widely used theory of convection is the mixing length theory (MLT; Böhm-Vitense 1958) described by the MLT parameter, α_{MLT}, which is the distance travelled by convective eddies before dissolving, in units of the pressure scale height, H_P. Additional prescriptions are needed to define the borders of convective zones (usually defined by the Schwarzschild or Ledoux criteria) and to treat the so-called overshooting process. The latter effect happens when a rising (sinking) eddy of plasma crosses the border of a convective zone due to its inertia, and is commonly described by the overshooting distance d_{ov}, in H_P units. Changes in the α_{MLT} and d_{ov} parameters will result in different evolutionary tracks, and different amounts of mixing of the chemical elements throughout the star, as it evolves. Hence, both effects can be calibrated to fit a variety of observations. The α_{MLT} parameter is usually calibrated with the Sun, and a fixed value is commonly adopted in stellar evolution codes (Weiss & Schlattl 2008; Brott et al. 2011b; Bressan et al. 2012; Choi et al. 2016; Spada et al. 2017; Hidalgo et al. 2018), although some codes use a slightly varying α_{MLT} depending on the stellar mass (Ekström et al. 2012).

Different approaches are used to constrain the d_{ov} parameter, using various types of data, such as colour–magnitude diagrams (CMDs) of star clusters (e.g. Woo et al. 2003; Rosenfield et al. 2017), bump Cepheids (Keller & Wood 2006), asteroseismology of either OB (Moravveji et al. 2015) or red clump (Bossini et al. 2017) stars, or detached double-lined eclipsing binaries (DLEBs; Stancliffe et al. 2015; Claret & Torres 2016; Valle et al. 2016; Claret & Torres 2017; Higl & Weiss 2017; Valle et al. 2017; Claret &

★ E-mail: gcosta@sissa.it

Torres 2018; Constantino & Baraffe 2018; Higl et al. 2018). A series of works (e.g. Demarque et al. 2004; Pietrinferni et al. 2004; Bressan et al. 2012; Mowlavi et al. 2012) suggest that there is a transition regime of the overshooting process: Its efficiency should grow from 0 for stars with radiative cores (initial mass $M_i \sim 1$–$1.2\,M_\odot$) up to a constant value for stars with a mass $M_i \geq 1.6$–$2\,M_\odot$. Stars in that constant range are considered to have a fully efficient overshooting process. This suggestion is reinforced by Claret & Torres (2016, 2017, 2018), who analyse the properties of 38 DLEBs to calibrate the strength of core overshooting, finding a clear indication for a plateau in the overshooting efficiency for masses $M_i > 2\,M_\odot$.

However, other studies using similar data do not find the same plateau. In particular, Stancliffe et al. (2015) model 12 EBs from the sample of Torres, Andersen & Giménez (2010), not finding any trend of the d_{ov} parameter with mass. Higl & Weiss (2017) studied a sample of stars mainly in the main-sequence phase, finding no strict constraint on the overshooting value. In a sequence of papers regarding a few specific systems, Valle et al. (2016, 2017) call attention to the increased errors when other variables, such as the initial helium content, are fitted together with the overshooting efficiency. More recently, Constantino & Baraffe (2018) analyse 8 binary systems selected from the 38 DLEBs in the Claret & Torres (2016, 2017, 2018) sample, finding a large dispersion in the results, even concluding that DLEBs cannot be used to constrain overshooting. Therefore, the DLEB results are still controversial.

In this paper we investigate the possible combined effect of core overshooting and rotation to explain the extra mixing suggested by the observed DLEBs. The paper is structured as follows. In Section 2 we describe the adopted DLEB data sample and the general method used for the statistical analysis. In Section 3 we describe how we have updated our PAdova-tRieste Stellar Evolution Code (PARSEC) to allow us to deal with mixing by rotation and overshooting. In Section 4 we perform the analysis using models with overshooting alone and we discuss the corresponding results. Since with overshooting alone we cannot fit the data with a fixed value of the overshooting parameter, we test the hypothesis, in Section 5, that rotation may cause the additional mixing required. We also derive a quantitative estimate of the initial rotational velocity required to fit the data. A discussion is presented and conclusions are drawn in Section 6.

2 DATA AND METHODS

2.1 DLEB data

The stars used in this paper are selected from the sample of detached double-lined eclipsing binaries studied by Claret & Torres (2016, 2017, 2018). The authors provide 38 DLEBs with very well-determined masses and radii, with uncertainties below 3 per cent, and also precise values of effective temperatures, with uncertainties below 6 per cent, and metallicity, with [Fe/H] absolute uncertainties below 0.2 dex. The stars are analysed by means of stellar evolution models that account for different mixing efficiencies, caused by different values of the core overshooting parameter (λ_{ov}; see Section 3.1), and by different initial rotational velocities. In both cases, various mixing efficiencies for models with a given mass and composition correspond to different locations in the Hertzsprung-Russel (HR) diagram and different evolutionary time-scales. The DLEB sample allows us to precisely test our models by comparison with the predicted location of both components in the HR diagram at a common time, which is that of the individual binary system. Our methodological approach is described below.

2.2 The Bayesian method

Given a star with a set of measured data y, the posterior probability distribution of their intrinsic quantities x can be expressed as

$$p(x|y) \sim p(y|x)p(x), \tag{1}$$

where the relationship between y and x, $y = \mathcal{I}(x)$, is given by a set of stellar models that spans the entire possible range of parameters; $p(y|x)$ is the likelihood function, which is the probability of the observed data y given a set of model parameters x; and $p(x)$ is the prior distribution, that is the distribution of how a given model parameter should behave. .Assuming that the measured data can be described as a normal distribution, with mean y' and standard deviation $\sigma_{y'}$, the likelihood function is

$$p(y'|x) = \prod_i \frac{1}{\sqrt{2\pi}\sigma_{y'}} \times \exp\left(\frac{-(y'_i - y_i)^2}{2\sigma^2_{y_i}}\right). \tag{2}$$

For each component in an eclipsing binary, we usually have as measured data

$$y = \{M, R, T_{\rm eff}, [{\rm Fe/H}]\}, \tag{3}$$

where the mass and radii come from the analysis of the light and velocity curve, whereas $T_{\rm eff}$ and [Fe/H] come from spectroscopic analysis of at least one of the components. We are primarily interested in determining the following parameters

$$x = \{t, \lambda_{ov}\}, \tag{4}$$

that is the stellar age (t) and the overshooting parameter (λ_{ov}). In our case, t is used only for a visual check of the best-fitting isochrones, whereas λ_{ov} is the parameter we are actually looking for.

We adopt as prior functions

(i) a flat prior on age t; that is, all ages between minimum and maximum values of 5×10^7 yr and 13×10^9 yr are assumed to be equally likely;

(ii) similarly, a flat prior on the overshooting parameter λ_{ov}, between the minimum and maximum values of 0 and 0.8;

(iii) an assumed mass distribution given by the initial mass function from Kroupa (2002).

We then implement this Bayesian method as an extension in the PARAM code, described by da Silva et al. (2006) and Rodrigues et al. (2014, 2017), to treat the binary measured data. As theoretical models, we use isochrones derived from stellar evolutionary tracks described in Section 4.1. Thus, the code computes the joint probability density function (JPDF) for each star in the sample, that is a 3D distribution map of t, λ_{ov}, and [Fe/H].

Since we are dealing with a binary system, we have an additional, powerful constraint: The age t and the metallicity [Fe/H] should be the same for both components. Therefore, we can compute the JPDFs separately for components 1 and 2, and hence combine the probabilities to get the constrained value of λ_{ov}. The common way to proceed is to assume that the two stars have the same λ_{ov}, either because they have almost the same mass or because the overshooting distance seems to saturate above a given initial mass, for stars with $M_i > 1.6$–$2\,M_\odot$. In this way the combined JPDF is simply $\mathrm{CJPDF}_{\rm binary} = \mathrm{JPDF}_1 \times \mathrm{JPDF}_2$ (as done by Valle et al. 2017). Using the CJPDF is equivalent to taking a sort of average between the two λ_{ov} of the two stars. However, we note that finding the trend

of the overshooting as a function of the mass should be a result of the study, and not a bias introduced by the adopted methodology. To prevent this bias we prefer to use a different procedure that, starting from the JPDF(λ_{ov},t) of each component, allows us to account also for the common age of the system, as described in the following.

(i) We first compute the marginalization of the JPDF$_i$(λ_{ov},t) on age, that is the sum of all λ_{ov} values, obtaining the probability density function of the age (PDF$_i$(t)) for both the stars.

(ii) We then obtain the *corrected* JPDF of one star as the product cJPDF$_i$(λ_{ov},t) = JPDF$_i$(λ_{ov},t) × PDF$_j$(t), where i and $j \neq i$ refer to any two components.

In this way, we obtain the new corrected cJPDFs of the two stars, by using only the common age of the binary system without any prior on the overshooting parameter. We assume that the best values for the age and the overshooting parameter for each component are the mode of the corresponding marginalized distributions. The credible interval (CI) associated with the best value is calculated as the shortest interval including the 68 per cent of each marginalized distribution, as suggested by Rodrigues et al. (2014).

We remark that the present approach is fundamentally different from the method recently applied by Constantino & Baraffe (2018). Ours is a fully Bayesian approach that weights every small piece of the derived isochrones according to its likelihood, eventually giving little weight not only to the stellar models that are far from the properties of the observed stars, but also to isochrone sections corresponding to fast evolutionary stages. This does not happen in the Constantino & Baraffe (2018) method, which gives equal weight to all models crossing the 1σ region of the observed values – which may explain the larger error bars they derive.

Before discussing the results obtained with this method, we introduce the new PARSEC code and the adopted evolutionary models in the next section.

3 PARSEC VERSION 2.0

As mentioned above, the current analysis makes use of PARSEC models with rotation. Since this is a new feature of our code we will briefly describe its implementation below together with other updated input physics.

3.1 The updated input physics

There are three major updates of the code with respect to the previous versions (extensively described in Bressan et al. 2012; Chen et al. 2014, 2015; Tang et al. 2014; Fu et al. 2018). The first two concern the nuclear reaction network and the mixing treatment:

Nuclear reactions. We updated the nuclear reaction network, which contains up to 30 isotopic elements from hydrogen to silicon, now solved with a fully implicit method. The method is much faster than the previously adopted one (explicit scheme); however, the latter can still be activated for comparison purposes.

Diffusive convection. In previous releases, convective zones were 'instantaneously' homogenized within an evolutionary time-step. In the present release, instead, the elements in the turbulent regions are mixed by solving a system of diffusion equations coupled with the nuclear reaction rates for each chemical element. It is known that this kind of treatment produces chemical profiles that fulfill the conditions imposed by the different time-scales, evolutionary, convective, and nuclear, the latter time-scale being dependent on the particular chemical element under consideration.

In this work, we adopt the Schwarzchild criterion (Schwarzschild 1958) to define the convective unstable regions. The diffusion coefficient in the convective region is computed within the MLT framework, $D_{conv} = (1/3)\, v\, l$, where $l = \alpha_{MLT} H_P$ is the mixing length and v is the velocity. In the overshooting region the velocity is computed with the ballistic approximation[1] (Maeder 1975; Bressan, Chiosi & Bertelli 1981), also known as penetrative overshooting. In this scheme, the overshooting parameter (actually $\lambda_{ov} \times H_P$) is the mean free path that can be travelled by bubbles in the full convective region before dissolving (i.e. also *across* the border of the unstable region). Convective elements are accelerated in the unstable region and decelerated in the stable overshooting zone. The acceleration imparted to convective elements is derived in the framework of the mixing length theory so that the corresponding velocity field can be obtained. For an easy comparison with other existing models in the literature we keep track of the overshooting distance, d_{ov}, that is the extension of the overshooting region above the Schwarzschild border, during the evolution. For example, during H-burning, we find that, approximately, $d_{ov}/H_P \simeq 0.5\lambda_{ov}$, with a small dependence on the initial stellar mass. During the He-burning phase, we adopt the same prescription. However, since as the helium burning proceeds the core grows, giving rise to a distinct molecular weight barrier and associated mixing phenomena like semiconvection and breathing pulses of convection, the above simple scaling loses its validity. Further discussion on the method can be found in Bressan, Bertelli & Chiosi (1986), where details on the core overshooting, during the central He-burning phase, are also given.

3.2 Implementation of rotation

The third update in the PARSEC V2.0 code concerns the implementation of rotation. This implementation will be described in detail in a separate paper (Costa et al. 2018, in preparation). Here we only provide a summary.

As is well known, rotating stars evolve differently from their corresponding non-rotating stars, in all main parameters such as luminosity, effective temperatures, lifetime of H- and He-burning phases, surface chemical abundances, and moreover in their final fates. All these different effects result from the interplay of two main physical factors: the departure from spherical geometry due to the centrifugal forces, and the enhancement of the chemical mixing and of the mass-loss rates.

3.2.1 Effects due to departure from spherical geometry

To include these effects into the stellar structure equations, preserving a 1D description of the problem, we follow the method outlined by Kippenhahn & Thomas (1970), which was further developed by Endal & Sofia (1976), Zahn (1992), and Meynet & Maeder (1997). We adopt the so-called shellular rotation law, which implies that the star is structured in shells that are isobars (surfaces with a constant value of pressure, P). Furthermore, the angular velocity is kept constant, Ω = const, along each isobar. This assumption is supported by the fact that the horizontal turbulent mixing in rotating stars is much stronger than the vertical one, which acts between two consecutive shells (Zahn 1992). Another basic assumption is the use of the Roche approximation, which allows us to compute the

[1] A treatment of convective overshooting similar to that described by Freytag, Ludwig & Steffen (1996) is also implemented, but it is not used in this work.

shape of the isobar surfaces and the effective gravity (the gravity plus the centrifugal forces along the surface). Meynet & Maeder (1997) show that using these prescriptions it is possible to adopt the modified 1D stellar structure equations by Kippenhahn & Thomas (1970) to model a differentially rotating star.

This scheme is currently adopted by most stellar evolutionary codes that treat rotation, such as MESA (Paxton et al. 2011, 2013, 2015, 2018), the Geneve stellar evolution code (Eggenberger et al. 2008), FRANEC (Chieffi & Limongi 2013, 2017), KEPLER (Heger & Langer 2000), STERN (Petrovic et al. 2005; Yoon & Langer 2005; Brott et al. 2011a), and now PARSEC v2.0.

3.2.2 Stellar structure equations with rotation

Within the Kippenhahn & Thomas (1970) and Meynet & Maeder (1997) scheme, the values of the physical quantities must be reinterpreted with respect to the classical one. In particular, for any quantity, q, that is not constant over an isobaric surface, an averaged value is used, and it is defined by

$$\langle q \rangle = \frac{1}{S_P} \int_{P=\text{const}} q \, \mathrm{d}\sigma, \tag{5}$$

where S_P is the total surface of the considered isobar and $\mathrm{d}\sigma$ is the surface element. Here, we report the modified equations of stellar structure for the convenience of the reader. The hydrostatic equilibrium equation reads

$$\frac{\partial P}{\partial M_P} = -\frac{G\,M_P}{4\pi\, r_P^4}\, f_P, \tag{6}$$

where M_P is the mass enclosed by an isobar, G is the gravitational constant, f_P is a form factor defined in equation (12), and r_P is the 'volumetric radius', defined by $V_P = \frac{4\pi}{3} r_P^3$, which is the volume inside an isobar. The continuity equation is

$$\frac{\partial r_P}{\partial M_P} = \frac{1}{4\pi\, r_P^2\, \overline{\rho}}, \tag{7}$$

where $\overline{\rho}$ is the average of the density over the volume between two isobars (see Meynet & Maeder 1997). The conservation of the energy is

$$\frac{\partial L_P}{\partial M_P} = \epsilon_\mathrm{n} - \epsilon_\nu + \epsilon_\mathrm{g}, \tag{8}$$

where ϵ_n, ϵ_ν, and ϵ_g are the rates of nuclear energy production, neutrino energy losses, and the gravitational energy rate, respectively. The equation of energy transport reads

$$\frac{\partial \ln \overline{T}}{\partial M_P} = -\frac{G\,M_P}{4\pi r_P^4}\,\frac{1}{P}\, f_P \,\min\left[\nabla_\mathrm{ad}, \nabla_\mathrm{rad}\frac{f_T}{f_P}\right], \tag{9}$$

with the temperature gradients

$$\nabla_\mathrm{ad} = \frac{P\delta}{\overline{T}\,\overline{\rho} c_P}, \tag{10}$$

$$\nabla_\mathrm{rad} = \frac{3}{16\pi acG}\,\frac{\kappa L_P\, P}{M_P}, \tag{11}$$

where $\delta = \left(\frac{\partial \ln \rho}{\partial \ln T}\right)_{P,\mu}$ is a thermodynamic derivative, c_P is the specific heat capacity, κ is the opacity, a is the radiation constant, and c is the speed of light. The form factors are

$$f_P = \frac{4\pi r_P^4}{G\,M_P S_P}\,\frac{1}{\left\langle g_\mathrm{eff}^{-1}\right\rangle}, \tag{12}$$

$$f_T = \left(\frac{4\pi r_P^2}{S_P}\right)^2 \frac{1}{\left\langle g_\mathrm{eff}^{-1}\right\rangle \langle g_\mathrm{eff}\rangle}, \tag{13}$$

where $\langle g_\mathrm{eff}\rangle$ is the surface average of the effective gravity, that is the sum of the centrifugal and gravitational forces. The form factors are dimensionless quantities that allow us to take into account the geometrical distortion of the star (due to rotation) in our system of equations. We also modified the atmospheric equations, using the prescriptions by Meynet & Maeder (1997).

3.2.3 Transport of angular momentum

Besides the geometrical distortion in the structure equations, we have included two rotational instabilities, the meridional circulation (know as 'the Eddington–Sweet circulation', a macro-motion of the material, from the poles to the equator or reverse, due to the thermal imbalance of a rotating star) and the shear instability (due to the friction between two consecutive shells of the star). These instabilities contribute to a redistribution of the angular momentum and chemical elements throughout the whole star, during the evolution. For the transport of angular momentum, we assume the pure diffusive approximation (Heger, Langer & Woosley 2000) and the equation of transport reads

$$\rho r^2 \frac{\mathrm{d}r^2\Omega_r}{\mathrm{d}t} = \frac{\partial}{\partial r}\left(\rho r^4 D \frac{\partial \Omega_r}{\partial r}\right), \tag{14}$$

where Ω_r is the angular velocity distribution along the star (at a given time-step), and with a total diffusion coefficient produced by the sum of the different rotation instabilities

$$D = D_\mathrm{mix} + D_\mathrm{s.i.} + D_\mathrm{m.c.} \tag{15}$$

where

(i) D_mix is the diffusion coefficient in the convective zones, computed with the MLT, and is non-zero only in the unstable zones of the star and in the overshooting region.

(ii) $D_\mathrm{s.i.}$ is the diffusion coefficient due to the shear instability. We use the formulation by Talon & Zahn (1997)

$$D_\mathrm{s.i.} = \frac{8}{5}\,\frac{\mathrm{Ri_c}\,(r\,\mathrm{d}\Omega_r/\mathrm{d}r)^2}{N_T^2/(K+D_\mathrm{h}) + N_\mu^2/D_\mathrm{h}}, \tag{16}$$

where the Brunt–Väisälä frequency has been split into $N_T^2 = \left(g\delta/H_p\right)(\nabla_\mathrm{ad} - \nabla_\mathrm{rad})$ and $N_\mu^2 = \left(g\varphi/H_p\right)\nabla_\mu$, $\mathrm{Ri_c} = 1/4$ is the critical Richardson number, $K = 4acT^3/3C_pk\rho^2$ is the thermal diffusivity, and $D_\mathrm{h} \simeq |rU|$ is the coefficient of horizontal turbulence (Zahn 1992).

(iii) $D_\mathrm{m.c.}$ is the diffusion coefficient due to the meridional circulation, and we use the approximation given by Zahn (1992):

$$D_\mathrm{m.c.} \simeq \frac{|rU|^2}{30 D_\mathrm{h}}, \tag{17}$$

where U is the radial component of the meridional circulation velocity. In the code we included three possible choices for U: (1) the simpler expression given by Kippenhahn, Weigert & Weiss (2011); (2) the same expression corrected by a 'stabilizing' circulation velocity due to the molecular weight barrier following Heger et al. (2000); and (3) an approximate form of the more general expression of Maeder & Zahn (1998), for stationary and uniform rotation, given by Maeder (2009) and Potter, Tout & Eldridge (2012). In this work, we use the latter prescription. Equation (17) is valid

when $D_h \gg D_{s.i.}$, so we are assuming that the Ω in a shell is 'instantaneously' homogenized (i.e.'shellular' approximation law).

The mixing of chemical elements induced by these instabilities is usually taken into account by expressing the total diffusion coefficient as a weighted sum of the different contributions:

$$D_{tot} = D_{mix} + f_c \times (D_{s.i.} + D_{m.c.}). \quad (18)$$

Here, the rotation diffusion coefficients are scaled by a factor f_c, used to calibrate the efficiency of the rotational extra mixing (the calibration of this parameter is discussed in the next section). It is worth mentioning that a more complete treatment should account for interactions between the above mixing processes that could possibly affect their efficiency, as described, for example, in Maeder et al. (2013). These effects are generally not included in the literature also because the total mixing coefficient already contains parameters that need to be calibrated on observations.

In each time-step, we conserve the angular momentum along the structure and in the atmosphere of the star, hence assuring the conservation of the total angular momentum with age. In this context, we recall that the parameter characterizing our evolutionary tracks regards the angular rotation rate, ω, that is the ratio between the angular velocity (Ω) and the break-up angular velocity (Ω_{crit}), at the stellar surface. A few models before the zero-age main sequence (ZAMS), the code computes the rotation rate Ω that corresponds to a given ω, and assigns this rotation uniformly throughout the star. This ingestion of initial angular momentum is completed before 1 per cent of hydrogen has been burned in the core. Afterwards, the current rotational velocity at the surface generally decreases as the star ages.

3.3 Calibration of parameters

Current implementations of rotation require the use of two parameters f_μ and f_c that control the molecular barrier 'strength' and the chemical mixing efficiency, respectively (Heger et al. 2000; Yoon & Langer 2005; Brott et al. 2011a; Potter et al. 2012; Chieffi & Limongi 2013; Paxton et al. 2013). The f_c parameter multiplies the rotational diffusion coefficients in the chemical diffusion equation as in equation (18). f_μ multiplies the molecular weight gradient; hence, the effective molecular gradient is

$$\nabla_\mu^{eff} = f_\mu \times \nabla_\mu. \quad (19)$$

The calibration of the mixing efficiency due to rotation is an open problem, and there are different ways to find acceptable values of these two parameters. For instance, the method used by Heger & Langer (2000) consists of setting up the two parameters to reproduce the ratio between the surface nitrogen abundance at the terminal age of main sequence (TAMS), and the ZAMS, for 10–20 $M_\odot$ stars of solar metallicity. This method was used for the calibration of the FRANEC code (Chieffi & Limongi 2013). A second method was developed by Brott et al. (2011a,b), who used the observed N surface abundances of a sample of stars from the Large Magellanic Cloud (LMC) VLT-FLAMES survey to calibrate their models. In this work, we compare the surface N enrichment ratio of massive stars with the corresponding models by Brott et al. (2011a). To be consistent in the comparison, we computed our models with a similar chemical partition, and with the same initial metallicity, as reported in Table 1. Our best values for the parameters, as a preliminary calibration, are $f_c = 0.17$ and $f_\mu = 0.45$. Table 2 shows the surface nitrogen enrichment ratios of our models compared with the values found by Brott et al. (2011a), for models with similar rotation rates in the ZAMS.

Table 1. Hydrogen (X), helium (Y), and metal (Z) mass fractions adopted for the models of massive stars in the Galaxy (MW) and in the Small and Large Magellanic Clouds (SMC, LMC), from Brott et al. (2011a).

	X	Y	Z
MW	0.7274	0.2638	0.0088
LMC	0.7391	0.2562	0.0047
SMC	0.7464	0.2515	0.0021

Table 2. Surface nitrogen enrichment ratio measured at the main-sequence termination, for different metallicities and masses, as predicted by PARSEC V2.0 with $f_c = 0.17$ and$f_\mu = 0.45$. Comparison values are from Brott et al. (2011a), for similar initial rotational velocities.

Mass ($M_\odot$)	$\frac{N_{sup}}{N^0_{sup}}$	
MW	PARSEC v2.0	Brott+11
12	3.87	3.25
15	4.66	2.65
30	13.31	13.55
LMC		
12	4.05	4.82
15	5.64	5.67
30	13.34	11.70
SMC		
12	5.52	6.27
15	6.82	9.39
30	13.93	16.16

4 THE EFFECT OF CORE OVERSHOOTING ALONE

We first assume that only core overshooting is responsible for the eventual extra mixing in intermediate-mass stars. The analysis of the data is performed using the corresponding non-rotating stellar evolutionary tracks with a varying overshooting parameter.

4.1 Evolutionary tracks and isochrones at varying overshooting parameter

For this purpose we computed different sets of evolutionary tracks, with a range of masses between 1 and 5 $M_\odot$ with the following values for the overshooting efficiency: $\lambda_{ov} = 0, 0.1, 0.2, 0.3, 0.4, 0.5, 0.6, 0.7, 0.8$. We adopt scaled solar mixtures based on Caffau et al. (2011) solar composition, with initial metal content $Z = 0.002, 0.004, 0.008, 0.014, 0.020$ and initial helium content given by $Y = \frac{\Delta Y}{\Delta Z} Z + Y_P = 1.78 \times Z + 0.2485$ (Table 3), as obtained from the solar calibration (Bressan et al. 2012). The corresponding values of [Fe/H] can be obtained using the relation [Fe/H] $\simeq$ [M/H] $= \log((Z/X)/0.0207)$ (Bressan et al. 2012) and are listed in Table 3. Finer grids of the evolutionary track in the parameters are obtained by interpolation. Tracks are interpolated within 'equivalent mass intervals' in which the evolution is similar, following the scheme described in Bertelli et al. (2008) for the case of grids of models computed at varying metal and helium

Table 3. *X*, *Y*, and *Z* mass fractions adopted for the models, and the correspondent [Fe/H] values.

X	*Y*	*Z*	[Fe/H]
0.746	0.252	0.002	−0.89
0.740	0.256	0.004	−0.58
0.729	0.263	0.008	−0.27
0.713	0.273	0.014	−0.02
0.696	0.284	0.020	+0.14

content. We refer to that paper for a detailed explanation – just recalling that, in our case, the varying helium content is replaced by a varying λ_{ov} (or ω with a fixed λ_{ov}; later in Sec. 5). Just to give a general idea of how this works, let us mention, as an example, that all tracks that develop a convective core in the MS and a degenerate core after the MS define one of 'equivalent interval of mass', even if their minimum and maximum masses, M_1 and M_2, occur at different values for different [Fe/H] and λ_{ov}. Tracks for intermediate values of [Fe/H] and λ_{ov} are interpolated, inside the mass range defined to be equivalent, by using the mass fraction inside this range, $(M - M_1)/(M_2 - M_1)$, as the independent variable. The interpolation between any two tracks then uses the concept of 'equivalent evolutionary sections' within the tracks: All stellar quantities are interpolated between pairs of evolutionary stages considered to be equivalent, using the age fraction inside these intervals as the independent variable. The whole process ensures a smooth interpolation between tracks. Interpolations performed for a given age then provide well-behaved isochrones. We also check that, by removing intermediate values of λ_{ov} from the interpolations, grids of interpolated tracks can be built for the same λ_{ov} that look very similar to the actually computed ones. This gives us confidence that the present grid of computed λ_{ov} values is sufficient for our goals.

We recall that mass loss is not taken into account, since we are dealing only with low- and intermediate-mass stars in the stages well below the tip of the red giant branch, for which no significant mass loss is expected to take place. Finally, we stress that a unique solar-model-calibrated mixing length parameter $\alpha_{MLT} = 1.74$ is adopted for all the computed evolutionary tracks, as in Bressan et al. (2012). Following their approach, we do not include the microscopic diffusion in stars that develop a convective core, hence in which the core overshooting process takes place. Since we are interested in studying such stars, even our $1\,M_\odot$ models are computed without the microscopic diffusion. We redirect the reader to Bressan et al. (2012) and Stancliffe et al. (2016) for a detailed comparison between models of low-mass stars with and without the microscopic diffusion.

4.2 Interpretation with models with overshooting

The HR diagram of Fig. 1 compares the observed data with some of the new tracks with a variable overshooting parameter, and the derived isochrones at a few selected ages. It shows that the range of parameters adopted for the models is wide enough to represent all the observed binary components.

After interpolating tracks for all the intermediate values of the two parameters *Z* and λ_{ov}, we used the corresponding isochrones to obtain the 3D JPDF of age, λ_{ov}, and [Fe/H] (as discussed in Section 2.2 for each star).

After verifying that the JPDF dependence on [Fe/H] has negligible effects on the results, we further decided to marginalize the 3D JPDFs on the metallicity, so obtaining a 2D JPDF on age and λ_{ov}. Two examples of the resulting 2D JPDF are shown in Fig. 2, specifically for the systems α Aurigae and TZ Fornacis.

To allow an easy comparison with previous studies (e.g. Valle et al. 2017), we first show the results obtained using the method of the combined JPDFs ($CJPDF_{binary}$), as described in Section 2.2. This method assumes not only that the binary stars must have the same age, but also that the agent of the extra mixing is the same. While the first assumption does not require further justification, the second condition is adopted because we are considering overshooting as the only source of extra mixing, and we will exclude from our discussion systems with mass ratios significantly different from unity, because overshooting may have a dependence on the stellar mass below a certain threshold mass.

The two plots show the superposition of three different JPDFs: one for the primary, one for the secondary, and the combined one. These three JPDFs are normalized to their respective peak values. The coloured regions delimit JPDF contour levels of 50 per cent (the darker), 10 per cent (the intermediate), and 1 per cent (the lighter) of the correspondent maximum density value. We stress that the values of these levels are arbitrarily chosen and do not correspond to the 2D credible intervals.

To assign best values and the correspondent credible intervals, we proceed as described in Section 2.2. Each map is marginalized in the two parameters to obtain two 1D probability distributions, one in age *t* and the other in λ_{ov}. The best values are the peak values (the mode) of the 1D marginalized distributions, while the credible interval of each parameter corresponds to the smallest interval around its mode corresponding to a probability of 68 per cent. The best values are represented by squares with the same darker colour of the corresponding 2D distribution.

The values of the λ_{ov} and age parameters we derive for α Aurigae and TZ Fornacis are listed in Table 4. Here, we show the parameters for the distributions of the individual components (superscript 1 and 2) and for the combined distribution (superscript C).

Applying the same method to all the binary systems in the sample, we obtain the results shown in Fig. 3, in which the λ_{ov} parameters of the combined distributions (CJPDFs) are plotted as a function of the *average mass* of each binary system.

The plot also shows the results found by Claret & Torres (2018) represented by their fit curve (their equation 2, the grey line). Their fit describes the overshooting efficiency by means of the parameter, f_{ov}, that enters the velocity scale height in the overshooting region. To plot this curve in Fig. 3, we first express their fit as a function of λ_{ov} using their relation between f_{ov} and their overshooting distance parameter ($\alpha_{ov} = d_{ov}/H_P$), $\alpha_{ov}/f_{ov} \sim 11.36$ (Claret & Torres 2017), and then we use our finding that $d_{ov}/H_P \simeq 0.5\lambda_{ov}$. The uncertainties introduced by this scaling process are well below the errors of the data. The darker and lighter grey areas describe the error bars of 0.003 and 0.004 (Claret & Torres 2018), respectively, multiplied by the same factors. The green area and the green line are the overshooting parameter adopted in Bressan et al. (2012). The overshooting parameter, which represents the extra mixing probed by our analysis, may depend on the initial mass, as found by other studies. From the comparison, we may identify two overshooting regimes in the plot: the growing one, in which overshooting increases from its null efficiency at about $M_i = 1\,M_\odot$ up to a mass of $\sim 1.5\,M_\odot$, and then the constant one, for larger masses, which indicates a regime of full efficiency. However, the big errors obtained in the low-mass range do not let us clearly identify the growing region. This growing efficiency with mass is commonly adopted by model builders (e.g. Demarque et al. 2004; Pietrinferni

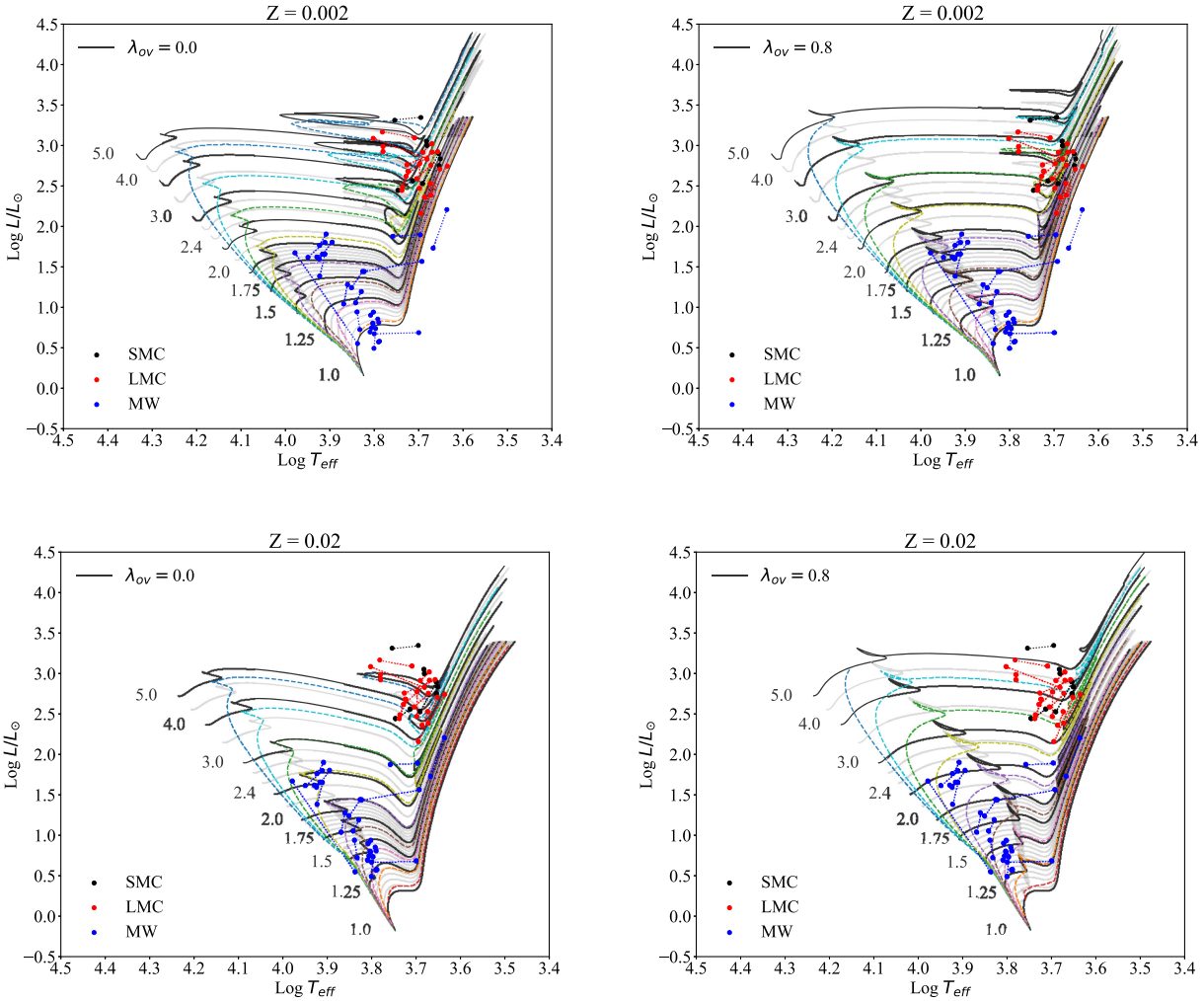

Figure 1. Overview of the data and models used in this work. The points linked by dotted lines are the stars in binaries, grouped into three broad metallicity bins (SMC, LMC, and MW, with black, red, and blue points respectively). Tracks and isochrones are overplotted, for the extreme values of metallicity and overshooting available: left-hand column for $\lambda_{ov} = 0.0$, right-hand column for $\lambda_{ov} = 0.8$, top row for $Z = 0.002$, bottom row for $Z = 0.02$. Tracks (the black and grey solid lines) cover the mass range from 1 to 5 $M_{\odot}$. The isochrones illustrated with dashed lines are equally spaced in $\log t$, covering the age range from 10^8 (upper blue dashed line) to 10^{10} yr (bottom red dashed line, in case of $Z = 0.02$).

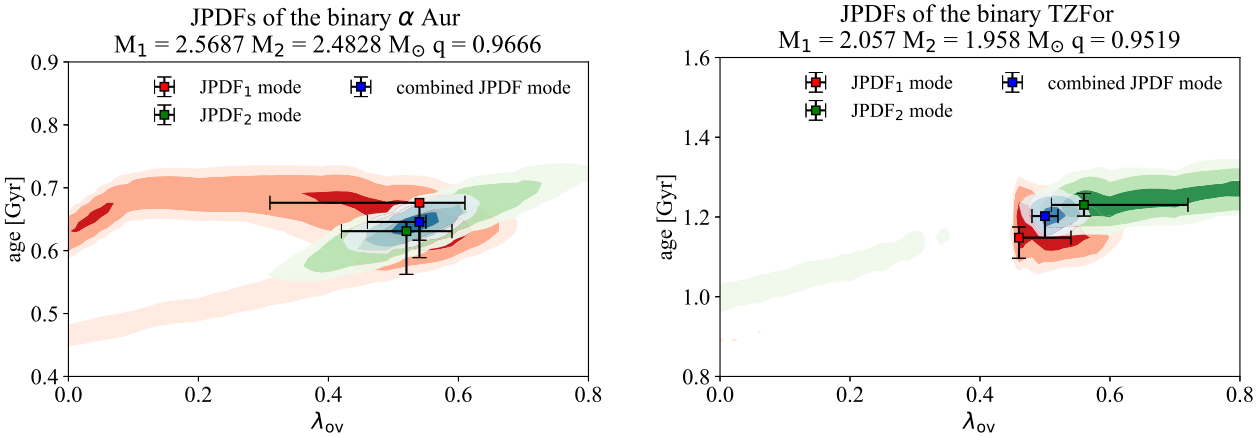

Figure 2. Two-dimensional JPDF maps as a function of the age, t, and the overshooting parameter, λ_{ov}, of the selected binary systems α Aurigae (left-hand panel) and TZ Fornacis (right-hand panel). The red (green) contours correspond to the primary (companion) star of the system, and the blue one is the CJPDF. The squares indicate the mode values of the corresponding coloured probability maps, with their related credible intervals (CIs).

Table 4. Resulting values of age and λ_{ov} for two selected binary systems.

Systems	α Aurigae	TZ Fornacis
M_1 ($M_\odot$)	2.5687 ± 0.0074	2.057 ± 0.001
M_2 ($M_\odot$)	2.4828 ± 0.0067	1.958 ± 0.001
JPDF mode values		
$\lambda_{ov}{}^1$	$0.54^{+0.07}_{-0.23}$	$0.46^{+0.08}_{-0.00}$
$\lambda_{ov}{}^2$	$0.52^{+0.07}_{-0.10}$	$0.56^{+0.16}_{-0.05}$
$\lambda_{ov}{}^C$	$0.54^{+0.01}_{-0.08}$	$0.51^{+0.01}_{-0.03}$
Age^1 (Gyr)	$0.676^{+0.001}_{-0.087}$	$1.15^{+0.03}_{-0.05}$
Age^2 (Gyr)	$0.631^{+0.015}_{-0.069}$	$1.23^{+0.03}_{-0.03}$
Age^C (Gyr)	$0.646^{+0.001}_{-0.029}$	$1.20^{+0.00}_{-0.05}$
Corrected JPDF mode values		
$\lambda_{ov}{}^1$	$0.55^{+0.07}_{-0.16}$	$0.46^{+0.07}_{-0.00}$
$\lambda_{ov}{}^2$	$0.54^{+0.06}_{-0.09}$	$0.55^{+0.10}_{-0.06}$
Age^1 (Gyr)	$0.65^{+0.02}_{-0.04}$	$1.23^{+0.00}_{-0.06}$
Age^2 (Gyr)	$0.65^{+0.02}_{-0.04}$	$1.23^{+0.00}_{-0.06}$

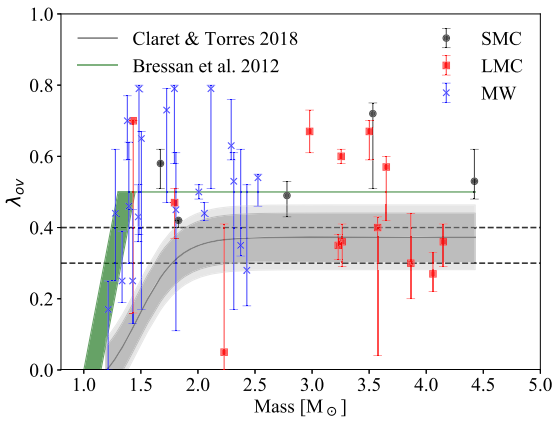

Figure 3. Resulting overshooting parameter λ_{ov} as a function of the stellar mass for the 38 DLEBs, obtained from the combined JPDF method. The best values (the modes) and the corresponding 68 per cent credible intervals are coloured with the same colour code as that used in Fig. 1, to divide stars of different galaxies. The black dashed lines are drawn for an easier reading. The grey line is the fit curve of the f_{ov} parameter found by Claret & Torres (2018) with the errors (grey areas) scaled by a multiplicative factor. The green line and area describe the λ_{ov} parameter used in Bressan et al. (2012). See the text for more details.

et al. 2004; Bressan et al. 2012; Mowlavi et al. 2012). The average scale of overshooting determined by this procedure, in the constant region, is $\lambda_{ov} = 0.5$.

However, the striking characteristic of the plot in Fig. 3 is that the overshooting parameter, in the full-efficiency regime, shows a large dispersion that is, in many cases, larger than the associated uncertainty. More specifically, our analysis of stars in binary systems suggests that the overshooting parameter for masses above about $M_i = 1.5\,M_\odot$ has a minimum value of $\lambda_{ov} = 0.3$–0.4, but at the same initial mass there can be values as large as the maximum value adopted in the models, $\lambda_{ov} = 0.8$. This dispersion is difficult to explain in the framework of the commonly used models of the overshooting process, which, in this regime, adopt a fixed efficiency. Furthermore, this result is also at variance with our previous assumption that justifies the combined JPDF, that is that the overshooting parameter is fixed in the full-efficiency regime. It is easy to repeat the analysis by relaxing this assumption and using only the condition on the age, as described in Section 2.2.

In Fig. 4 we show, as an example, how the JPDF contour maps change when we adopt this new method for the α Aurigae system. In the top panels we show the single-star JPDFs obtained from the param code, before applying the condition on the age. In the bottom panels we show the corrected JPDFs (cJPDFs) resulting from the application of the common age constraint. These corrected distributions have independent λ_{ov} parameters but share the same age distribution. The best values of the corrected JPDF distributions for α Aurigae and TZ Fornacis are shown in the bottom part of Table 4.

To show the effect of this new method, we repeat the statistical analysis for all the stars of the sample, and plot the λ_{ov} parameter as a function of the mass in Fig. 5.

The latter is similar to Fig. 3, but in this case each star has its own mass and λ_{ov} parameter. The dispersion of the points is similar to the one obtained with the CJPDF method, and again, there are several cases in which the values of λ_{ov} are not unique in a given mass bin, in particular looking at masses larger than $\sim$1.5 $M_\odot$. The credible intervals, in Fig. 5, are slightly larger than those plotted in Fig. 3.

As a further check we perform another analysis assuming a constant value of [Fe/H] for stars belonging to the same galaxies. This allows us to check how the metallicity affects the observed dispersion in λ_{ov}. Averaging the observed values of stars in different groups we obtain [Fe/H] $= -0.89 \pm 0.15$, -0.48 ± 0.1, and -0.14 ± 0.1 for the stars belonging to the SMC, LMC, and MW, respectively. The results of the analysis performed with mean [Fe/H] values are shown in Fig. 6. The plot is not significantly different from the former one. Some stars have different values of λ_{ov}, but the global trend remains very similar.

We note that, in all cases, the error bars at the lower mass end are larger than those associated with the higher masses. This is likely due to the fact that the lower mass sample contains several stars that are still on the early main sequence where the effects of overshooting are less evident and thus the models degenerate more.

In summary our analysis shows the following results.

1. In the mass range below 1.5 $M_\odot$, the λ_{ov} distribution populates all values explored in the analysis (from $\lambda_{ov} = 0.0$ to $\lambda_{ov} = 0.8$), and it is not possible to find a clear trend as a function of the mass.
2. In the mass range above 2 $M_\odot$, the λ_{ov} parameter shows a large scatter, even for similar initial masses. For these stars we find an average value of $\lambda_{ov} \sim 0.45$.
3. In this latter range, there is also an evident lack of points below $\lambda_{ov} \sim 0.3$–0.4, in agreement with the Claret & Torres (2018) distribution. The only points to populate this region (in Fig. 5) are the two components of OGLE-LMC-ECL-25658 at $M_i \simeq 2.23$, for which the derived λ_{ov} present extremely large error bars, and the secondary of OGLE-051019.64–685812.3, with $M_i = 3.179 \pm 0.028$ and $\lambda_{ov} = 0.11^{0.12}_{0.11}$, which is only marginally inconsistent with the $\lambda_{ov} > 0.3$ limit. In contrast, the sample presents 52 other stars with $M_i \geq 1.5\,M_\odot$ and derived $\lambda_{ov} > 0.3$.

The dispersion we find is certainly larger than that obtained by Claret & Torres (2017, 2018), who analysed the same data with different models and a different procedure. However, it is important to note that, in their analysis, they allow the mixing length parameter,

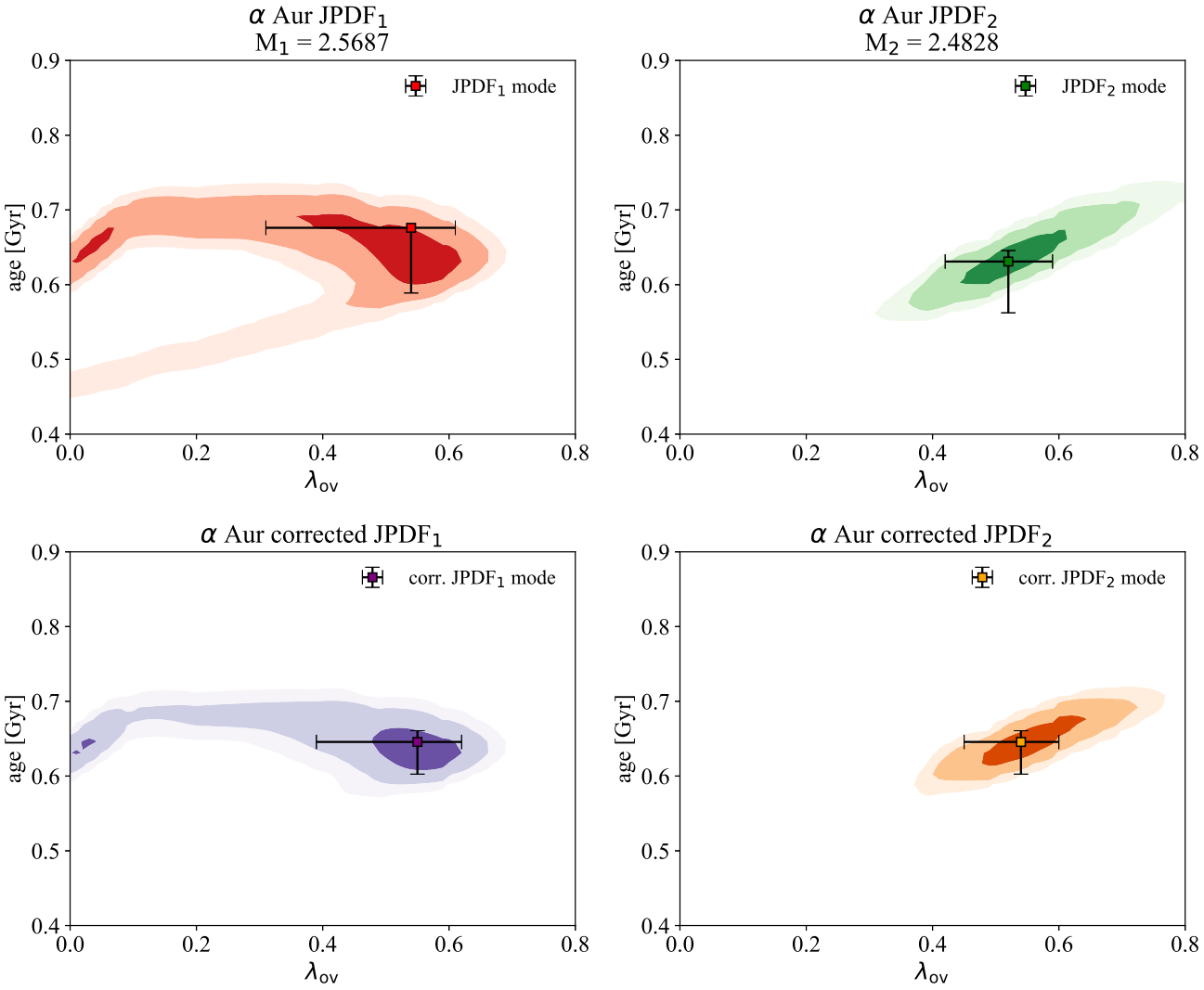

Figure 4. Selected JPDFs as a function of the age, t, and the overshooting parameter, λ_{ov}, for the two stars of the binary system α Aurigae. In the top panels there are two single-star JPDFs, as in Fig. 2. In the bottom panels there are new corrected JPDFs that constrain the age of the system, as described in the text. The purple (orange) contours represent the primary (companion) star corrected JPDF. The points indicate the maximum of the marginalized distribution with their corresponding CIs.

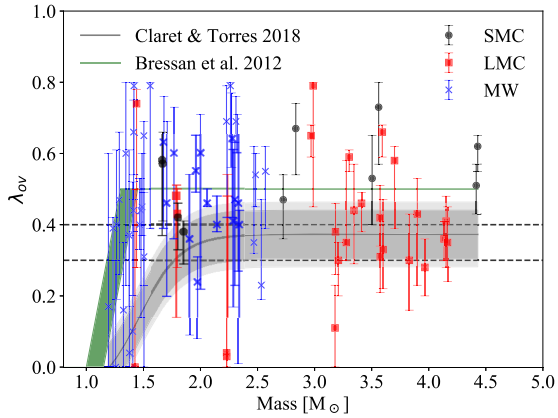

Figure 5. Same as Fig. 3, but with the new method to constrain the age of the system. Thus, the overshooting parameter λ_{ov} is shown as a function of the stellar mass for each star of our sample.

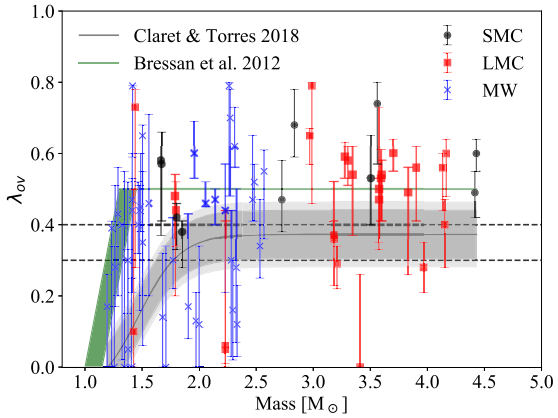

Figure 6. Same as Fig. 5, but showing results from the statistical analysis using the averaged metallicity for stars of the three different galaxies.

α_{MLT}, to change and their best fits are characterized by a significant star-to-star variation in the adopted α_{MLT}. This likely absorbs some of the scatter that we find in our results with a fixed α_{MLT}. A star-to-star scatter of the α_{MLT} is surprising and at variance with common findings from both observational and theoretical sides (Weiss & Schlattl 2008; Ekström et al. 2012; Magic, Weiss & Asplund 2015; Arnett et al. 2018). On the other hand, a large scatter of λ_{ov} at the same initial mass is difficult to explain within the current convection theories that adopt fixed values for the mixing parameters (including the MLT).

We speculate here that the observed scatter above the minimum threshold, suggested by our analysis, is a signature of an additional source of extra mixing on top of that caused by core overshooting. The most natural candidate is stellar rotation because it is known to be a source of extra mixing and it has a stochastic nature since stars with similar masses may rotate at different speeds. In the next section we will explore the additional effect of rotation.

5 EFFECTS OF ROTATION

In the previous section we have shown that the values of λ_{ov} in Figs 3, 5, and 6 are suggestive of a minimum overshooting parameter between 0.3 and 0.4, for stars with $M_i \geq 1.5\,M_\odot$. We have also argued that the excess mixing clearly shown by data above this overshooting threshold could be due to another effect that we speculate to be the rotational mixing. Here, we check this hypothesis by means of the new rotation models of PARSEC. However, we restrict our study to stars with mass greater than $1.9\,M_\odot$ because, being in advanced phases of evolution, they should have experienced the induced mixing by rotation during the previous hydrogen-burning phase. Some of these stars are in core He burning (CHeB) and, as mentioned in Section 3.1, the overshooting is treated in the same way as in the H-burning phase. Never the less, the core overshooting process in this phase is less critical, since what matters is the core mass at which stars enter into the CHeB phase, which is determined by the overshooting on the main sequence. Moreover, since they should be slow rotators now, they should not be significantly affected by geometrical distortions and their position in the HR diagram should not depend on the inclination of their rotation axes with respect to the line of sight.[2]

5.1 Evolutionary models with rotation

To study the combined effect of overshooting and rotation, we have computed sets of models with masses between 1 and $5\,M_\odot$, with a fixed overshooting efficiency of $\lambda_{ov} = 0.4$. This value of λ_{ov} is only a preliminary choice dictated, on one side, by the paucity of stars below this value (see e.g. Fig. 5) and, on the other, by the large values derived for a few objects in the previous analysis. Concerning rotation (see Section 3.2), we explore a wide range of initial rotation rate parameters $\omega = 0.0, 0.1, 0.2, 0.3, 0.4, 0.5, 0.6, 0.65, 0.70, 0.75, 0.80$, at the ZAMS. All the other stellar evolution parameters are kept unchanged. As in the previous analysis, the grids of stellar tracks are interpolated to produce finer grids of tracks as a function of [Fe/H] and ω. Selected sets of tracks with different values of ω and overshooting are shown in Fig. 7. In the left-hand panels, we show the tracks with a constant value of $\lambda_{ov} = 0.4$, with and without rotation, overplotted to the data. The selected rotation rate is $\omega = 0.6$. In the right-hand panels, we compare tracks with large overshooting, $\lambda_{ov} = 0.8$, and without rotation, with tracks with $\lambda_{ov} = 0.4$ and with $\omega = 0.6$. This figure allows us to make an immediate comparison between the effects of large overshooting and those of mild overshooting and rotation. For example, we see that, for the above parameters, the non-rotating tracks of $M_i = 5\,M_\odot$ and $M_i = 4\,M_\odot$ run almost superimposed in the HR diagram to their corresponding models with mild overshooting and rotation. This already suggests that objects for which we have determined a large overshooting parameter without rotation could be simply explained by mild overshooting and additional rotational mixing. In support of this suggestion we show, in Fig. 8, the evolution of the border of the convective core (in mass fraction) during the hydrogen-burning phase, for the models with 2, 2.6, and $4\,M_\odot$ and for two metallicities ($Z = 0.002$ and 0.014). In each panel there are three models with core overshooting and no rotation (the solid lines) and three models with a fixed λ_{ov} parameter ($\lambda_{ov} = 0.4$) and different rotation rates (ω, the dashed lines), as indicated in the figure. We note that the sizes of the cores of the models with fixed overshooting ($\lambda_{ov} = 0.4$) and varying initial rotational velocities decrease more slowly than those of the corresponding model without rotation. This effect is more pronounced for larger rotational velocities and for larger masses. It also depends slightly on the metallicity. For both the metallicities, in the case of $M_i = 4\,M_\odot$, the final core of the fastest rotating model becomes larger than that of the non-rotating model with $\lambda_{ov} = 0.8$. This effect is due to the increase of the mean molecular weight induced by rotational mixing, which directly affects the stellar luminosity. This effect is less evident in models with masses below about $2\,M_\odot$, which instead, are more sensitive to the overshooting process. Eventually, larger rotation rates are needed to obtain bigger effects. In the case of $Z = 0.014$ and $M_i = 2\,M_\odot$, the age differences (Δage) are still appreciable. In particular, at the end of the main sequence, the Δage between the model with $\lambda_{ov} = 0.4$ and without rotation and the model with $\lambda_{ov} = 0.4$ and $\omega = 0.8$ is $\sim$24 Myr.

These facts are in line with our choice to restrict our study to stars with mass greater than $1.9\,M_\odot$. In the next section we show the results of the statistical analysis performed with the new models with rotation, in this mass range.

5.2 Results

In Section 4.2 we applied the Bayesian analysis to obtain the JPDF of age and λ_{ov} parameters for the components of our binary systems. Here we repeat the same procedure for the models with fixed overshooting, $\lambda_{ov} = 0.4$, and variable rotation parameter, ω. Moreover, we limit the analysis to initial masses $M_i \geq 1.9\,M_\odot$ because our goal is to study the effects of rotation in the mass range where overshooting has eventually reached its maximum efficiency. This simplifies our problem because it allows us to work with only two independent parameters, age and ω, since λ_{ov} is fixed. The result of this analysis is displayed in Fig. 9. In the figure we plot for each component the derived mode and credible intervals (CIs) of the initial ω as a function of the initial mass. In this analysis we have adopted the observed values of [Fe/H]. A similar plot, but made adopting the average value of [Fe/H] for each group of binary stars depending on the parent galaxy, is shown in Fig. 10. To better compare the results obtained adopting variable overshooting in one case and fixed overshooting plus rotation in the other case, we also list in Table 5 the derived parameters for the analysed binary components, in the two cases. We see that, independently from the

[2]This was verified a posteriori; see for instance the cases of α Aurigae and TZ Fornacis commented on in Section 6.

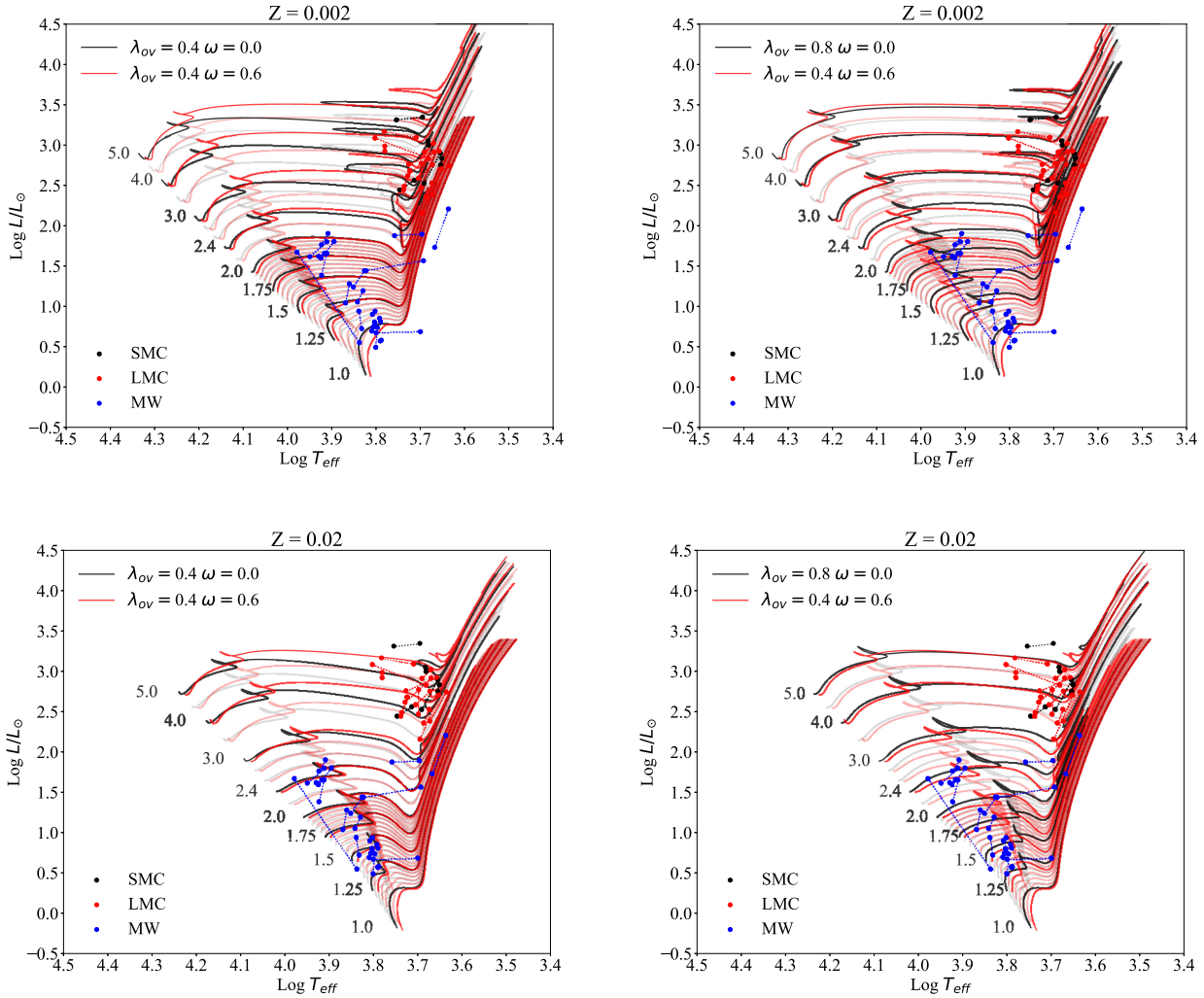

Figure 7. Overview of the data and evolutionary tracks with rotation used in this work. The points united by the dotted lines are the stars in binaries, grouped as in Fig. 1. Tracks with fixed $\lambda_{ov} = 0.4$ without rotation (in black), and with rotation, with $\omega = 0.6$ (in red) are overplotted, for the extreme values of metallicity in the left-hand column. In the right-hand column, tracks with $\lambda_{ov} = 0.4$ and $\omega = 0.6$ (in red) are overplotted with tracks with $\lambda_{ov} = 0.8$ without rotation (in black). All the sets of tracks cover the mass range from 1 to 5 $M_{\odot}$. All intermediate values of ω and Z are available. We recall that tracks with rotation and $M_i < 1.9\,M_{\odot}$ are not used in the analysis.

method used to determine the metallicity, rotation is actually able to explain the varying extra mixing observed in stars with similar masses. The results show a certain degree of stochasticity that now can be simply explained by different initial rotational rates, from very small to quite large values. We remind the reader that in objects with very small initial rotational rates the extra mixing is produced only by mild core overshooting ($\lambda_{ov} = 0.4$). On the other hand, objects that in the previous analysis required a high overshooting mixing are now well fitted by high rotational rates on top of the same amount of overshooting ($\lambda_{ov} = 0.4$).

Concerning the ages, the other parameter derived from our analysis, we note that they are almost independent of the adopted mixing scheme used in the models to match the stellar properties (see Table 5). The largest difference in the ages is $|\delta_{Age}/Age_{\omega}| \sim 12$ per cent, for the system TZ Fornacis (without taking into account the OGLE-LMC-ECL-25658 and OGLE-051019.64–685812.3 systems, which are evident outliers) but, in general, the average difference is below ∼5 per cent. Thus, the two different mixing schemes are actually able to reproduce the same radius, $T_{\rm eff}$, mass, and age as those of an observed star, indicating that, at the end, they produce the same global mixing.

6 DISCUSSION AND CONCLUSIONS

In this paper, we analyse the concurrence between convective core overshooting and rotation in low- and intermediate-mass stars. Both processes may cause extended extra mixing in the central regions of the stars. There is a large debate in the literature concerning the efficiency of these two processes. While overshooting is widely recognized as an important process affecting the evolution of all stars with sizable convective cores (as well the ages assigned to all stellar populations up to ages of a few Gyr), rotation has been considered relatively less important, at least for low- and intermediate-mass stars. There is growing evidence, however, that fast rotators are reasonably common and may significantly affect the CMDs of young and intermediate-age clusters in the Magellanic

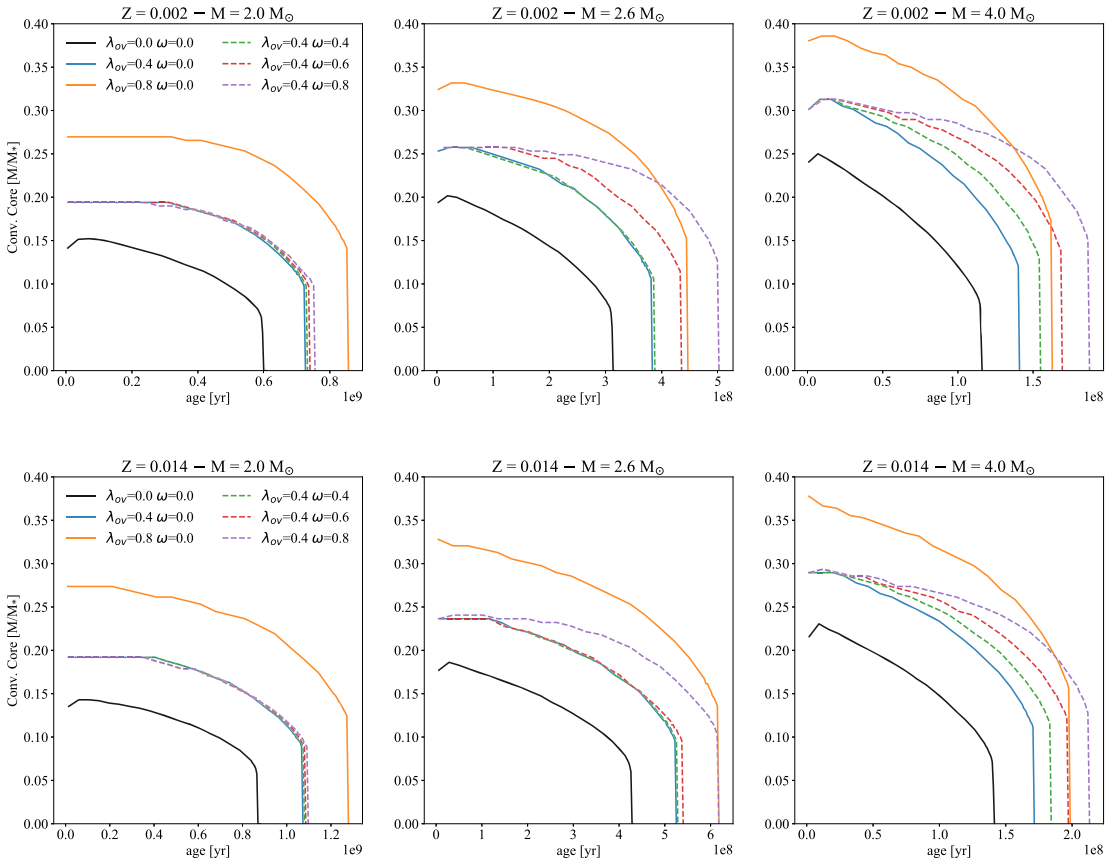

Figure 8. Comparison between the convective core extension (mass fraction) versus time (year) of different models. The solid lines are models with a varying overshooting parameter (λ_{ov} = 0.0, 0.4, 0.8) and no rotation, while the dashed lines are models with a fixed overshooting parameter (λ_{ov}= 0.4) and varying rotation (ω = 0.4, 0.6, 0.8). In the top panels there are models with masses of 2, 2.6, and 4 $M_{\odot}$ (left- to right-hand panels), with a metallicity content of Z = 0.002. In the bottom panel are models with Z = 0.014.

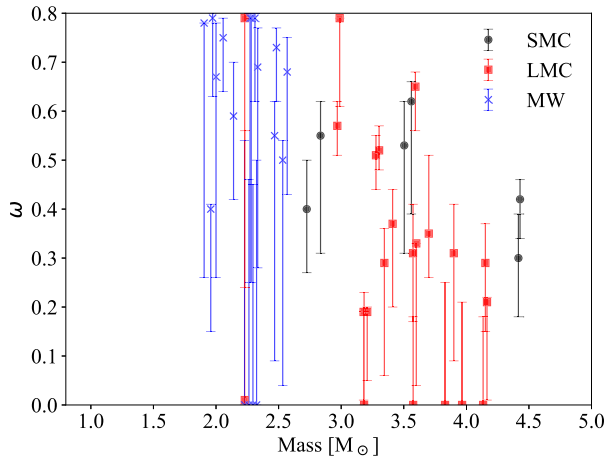

Figure 9. Resulting initial angular rotation rate, ω, as a function of the initial stellar mass for the stars with $M_i \geq 2.0\,M_{\odot}$, with the correspondent 68 credible interval bars. The colour code and the symbols are the same as in Fig. 3. Results from the analysis performed with the observed [Fe/H] values.

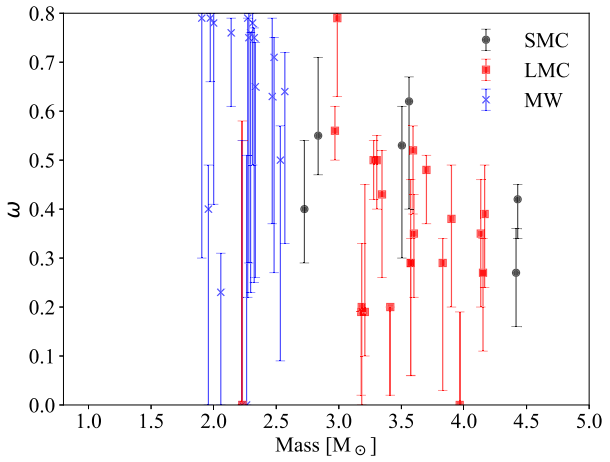

Figure 10. Same as Fig. 9, but in this case the analysis has been performed with the averaged [Fe/H] for stars of each galaxy.

Clouds and in the Galaxy (see e.g. Brandt & Huang 2015; Marino et al. 2018a, b). Here we aim at shedding light on the relative importance of these two processes by analysing a sample of well-studied double-lined eclipsing binaries. The accurate determinations of their masses, radii, luminosities, effective temperatures, and metallicities, together with the constraint imposed by the common ages of the systems, provide a unique opportunity to test stellar evolution models with different mixing schemes. For this purpose we consider the two most common extra mixing schemes, overshooting and rotational mixing. We adopt a Bayesian approach that allows us to

Table 5. Resulting values of the overshooting parameter and the age of the system, for the two types of analysis. First analysis: interpretation with only the overshooting parameter, λ_{ov}. Second analysis: interpretation with a fixed value of the overshooting parameter, $\lambda_{ov} = 0.4$, and variable rotation. For each binary system component is listed the observed values of mass and [Fe/H] (from Claret & Torres 2017, 2018), and the computed best values of the λ_{ov} and age parameters (for the two analysis) with their corresponding errors. In the last column there is the relative absolute difference (in percentage) between the age parameters found in the two different analyses. In the Table we represent cells with no value using dashes, while the three dots are used to represent the same value of the cell above.

			Variable overshooting		Fixed overshooting and rotation		
Binary name	Mass ($M_\odot$)	[Fe/H]	λ_{ov}	Age$_{\lambda_{ov}}$ (Gyr)	ω	Age$_\omega$ (Gyr)	$\lvert\delta$ Age/Age$_\omega\rvert$ (%)
SMC-108.1–14904	4.429 ± 0.037	-0.80 ± 0.15	$0.62^{+0.02}_{-0.09}$	$0.132^{+0.000}_{-0.009}$	$0.42^{+0.04}_{-0.08}$	$0.135^{+0.000}_{-0.009}$	2.3
...	4.416 ± 0.041	...	$0.51^{+0.06}_{-0.08}$	...	$0.30^{+0.09}_{-0.12}$	...	...
OGLE-LMC-ECL-CEP-0227	4.165 ± 0.032	–	$0.35^{+0.10}_{-0.11}$	$0.141^{+0.021}_{-0.003}$	$0.21^{+0.01}_{-0.20}$	$0.145^{+0.003}_{-0.003}$	2.2
...	4.134 ± 0.037	–	$0.36^{+0.05}_{-0.06}$	...	$0.00^{+0.18}_{-0.00}$	...	...
OGLE-LMC-ECL-06575	4.152 ± 0.030	-0.45 ± 0.10	$0.41^{+0.07}_{-0.13}$	$0.151^{+0.004}_{-0.013}$	$0.29^{+0.08}_{-0.14}$	$0.159^{+0.004}_{-0.007}$	4.5
...	3.966 ± 0.032	...	$0.28^{+0.08}_{-0.08}$	...	$0.00^{+0.21}_{-0.00}$	...	...
OGLE-LMC-ECL-CEP-2532	3.900 ± 0.100	–	$0.43^{+0.10}_{-0.20}$	$0.170^{+0.008}_{-0.025}$	$0.31^{+0.10}_{-0.22}$	$0.178^{+0.008}_{-0.012}$	4.5
...	3.830 ± 0.100	–	$0.30^{+0.14}_{-0.13}$	...	$0.00^{+0.25}_{-0.00}$	...	...
LMC-562.05–9009	3.700 ± 0.030	–	$0.58^{+0.04}_{-0.19}$	$0.195^{+0.014}_{-0.009}$	$0.35^{+0.16}_{-0.09}$	$0.200^{+0.019}_{-0.005}$	2.3
...	3.600 ± 0.030	–	$0.33^{+0.14}_{-0.11}$	...	$0.33^{+0.00}_{-0.29}$	...	...
OGLE-LMC-ECL-26122	3.593 ± 0.055	-0.15 ± 0.10	$0.66^{+0.02}_{-0.07}$	$0.263^{+0.006}_{-0.018}$	$0.65^{+0.03}_{-0.09}$	$0.282^{+0.000}_{-0.036}$	6.7
...	3.411 ± 0.047	...	$0.46^{+0.04}_{-0.07}$	...	$0.37^{+0.07}_{-0.17}$	...	...
OGLE-LMC-ECL-01866	3.574 ± 0.038	-0.70 ± 0.10	$0.42^{+0.09}_{-0.08}$	$0.200^{+0.009}_{-0.005}$	$0.31^{+0.10}_{-0.14}$	$0.209^{+0.020}_{-0.005}$	4.5
...	3.575 ± 0.028	...	$0.31^{+0.10}_{-0.10}$	...	$0.00^{+0.18}_{-0.00}$	...	...
OGLE-SMC-113.3–4007	3.561 ± 0.025	–	$0.73^{+0.07}_{-0.16}$	$0.214^{+0.010}_{-0.010}$	$0.62^{+0.04}_{-0.23}$	$0.234^{+0.035}_{-0.021}$	8.8
...	3.504 ± 0.028	–	$0.53^{+0.12}_{-0.13}$	...	$0.53^{+0.09}_{-0.22}$	...	...
OGLE-LMC-ECL-10567	3.345 ± 0.040	-0.81 ± 0.20	$0.44^{+0.13}_{-0.15}$	$0.246^{+0.018}_{-0.011}$	$0.29^{+0.07}_{-0.23}$	$0.246^{+0.018}_{-0.006}$	0.0
...	3.183 ± 0.038	...	$0.38^{+0.08}_{-0.12}$	...	$0.00^{+0.23}_{-0.00}$	...	...
OGLE-LMC-ECL-09144	3.303 ± 0.028	-0.23 ± 0.10	$0.59^{+0.03}_{-0.03}$	$0.302^{+0.000}_{-0.014}$	$0.52^{+0.05}_{-0.04}$	$0.302^{+0.007}_{-0.007}$	0.0
...	3.208 ± 0.026	...	$0.30^{+0.03}_{-0.13}$	...	$0.19^{+0.01}_{-0.14}$	...	...
OGLE-051019.64–685812.3	3.278 ± 0.032	–	$0.35^{+0.23}_{-0.05}$	$0.240^{+0.036}_{-0.026}$	$0.51^{+0.04}_{-0.07}$	$0.302^{+0.029}_{-0.007}$	21
...	3.179 ± 0.028	–	$0.11^{+0.12}_{-0.11}$	...	$0.19^{+0.00}_{-0.18}$	...	...
OGLE-LMC-ECL-09660	2.988 ± 0.018	-0.44 ± 0.10	$0.79^{+0.01}_{-0.34}$	$0.372^{+0.000}_{-0.017}$	$0.79^{+0.00}_{-0.18}$	$0.389^{+0.028}_{-0.018}$	4.5
...	2.969 ± 0.020	...	$0.65^{+0.02}_{-0.08}$	...	$0.57^{+0.05}_{-0.06}$	...	...
SMC-101.8–14077	2.835 ± 0.055	-1.01 ± 0.15	$0.67^{+0.06}_{-0.14}$	$0.380^{+0.000}_{-0.034}$	$0.55^{+0.07}_{-0.24}$	$0.372^{+0.009}_{-0.025}$	2.3
...	2.725 ± 0.034	...	$0.47^{+0.07}_{-0.11}$	...	$0.40^{+0.10}_{-0.13}$	...	...
α Aur	2.569 ± 0.007	-0.04 ± 0.06	$0.55^{+0.07}_{-0.16}$	$0.646^{+0.015}_{-0.043}$	$0.68^{+0.07}_{-0.25}$	$0.646^{+0.000}_{-0.083}$	0.0
...	2.483 ± 0.007	...	$0.54^{+0.06}_{-0.09}$	...	$0.73^{+0.04}_{-0.11}$	...	...
WXCep	2.533 ± 0.050	–	$0.23^{+0.24}_{-0.04}$	$0.562^{+0.013}_{-0.049}$	$0.50^{+0.04}_{-0.46}$	$0.550^{+0.000}_{-0.060}$	2.3
...	2.324 ± 0.045	–	$0.46^{+0.25}_{-0.19}$	...	$0.00^{+0.50}_{-0.00}$	...	...
V1031Ori	2.468 ± 0.018	–	$0.35^{+0.27}_{-0.03}$	$0.631^{+0.015}_{-0.042}$	$0.55^{+0.07}_{-0.46}$	$0.617^{+0.000}_{-0.041}$	2.3
...	2.281 ± 0.016	–	$0.41^{+0.20}_{-0.24}$	...	$0.79^{+0.00}_{-0.54}$	...	...
V364Lac	2.333 ± 0.014	–	$0.35^{+0.14}_{-0.28}$	$0.646^{+0.000}_{-0.070}$	$0.69^{+0.08}_{-0.41}$	$0.631^{+0.030}_{-0.014}$	2.3
...	2.295 ± 0.024	–	$0.47^{+0.15}_{-0.25}$	...	$0.00^{+0.45}_{-0.00}$	...	...
SZCen	2.311 ± 0.026	–	$0.70^{+0.07}_{-0.09}$	$0.708^{+0.017}_{-0.047}$	$0.79^{+0.01}_{-0.17}$	$0.692^{+0.016}_{-0.031}$	2.3
...	2.272 ± 0.021	–	$0.62^{+0.15}_{-0.20}$	...	$0.79^{+0.01}_{-0.54}$	...	...
OGLE-LMC-ECL-25658	2.230 ± 0.019	-0.63 ± 0.10	$0.03^{+0.51}_{-0.03}$	$0.676^{+0.100}_{-0.060}$	$0.01^{+0.55}_{-0.01}$	$0.631^{+0.163}_{-0.000}$	7.1
...	2.229 ± 0.019	...	$0.04^{+0.44}_{-0.04}$	...	$0.79^{+0.01}_{-0.55}$	...	...
V885Cyg	2.228 ± 0.026	–	$0.70^{+0.09}_{-0.28}$	$0.759^{+0.054}_{-0.034}$	$0.00^{+0.54}_{-0.00}$	$0.708^{+0.033}_{-0.016}$	7.2
...	2.000 ± 0.029	–	$0.60^{+0.12}_{-0.37}$	...	$0.67^{+0.11}_{-0.41}$	...	...
AIHya	2.140 ± 0.038	–	$0.40^{+0.09}_{-0.01}$	$1.047^{+0.024}_{-0.047}$	$0.59^{+0.11}_{-0.17}$	$1.023^{+0.024}_{-0.023}$	2.3
...	1.973 ± 0.036	–	$0.24^{+0.07}_{-0.16}$	...	$0.79^{+0.01}_{-0.16}$	...	...
AYCam	1.905 ± 0.040	–	$0.36^{+0.18}_{-0.27}$	$1.097^{+0.026}_{-0.142}$	$0.78^{+0.00}_{-0.52}$	$1.047^{+0.101}_{-0.024}$	4.7
...	1.709 ± 0.036	–	$0.46^{+0.23}_{-0.26}$	...	–	...	...
SMC-130.5–04296	1.854 ± 0.025	-0.88 ± 0.15	$0.38^{+0.03}_{-0.11}$	$1.047^{+0.024}_{-0.047}$	–	–	–
...	1.805 ± 0.027	...	$0.42^{+0.03}_{-0.09}$	...	–	–	–
OGLE-LMC-ECL-03160	1.799 ± 0.028	-0.48 ± 0.20	$0.40^{+0.10}_{-0.11}$	$1.122^{+0.053}_{-0.099}$	–	–	–

Table 5 – *continued*

Binary name	Mass ($M_\odot$)	[Fe/H]	Variable overshooting λ_{ov}	Variable overshooting Age$_{\lambda_{ov}}$ (Gyr)	Fixed overshooting and rotation ω	Fixed overshooting and rotation Age$_\omega$ (Gyr)	Fixed overshooting and rotation $\lvert\delta$ Age/Age$_\omega\rvert$ (%)
...	1.792 ± 0.027	...	$0.48^{+0.03}_{-0.34}$	...	–	–	–
EICep	1.772 ± 0.007	–	$0.60^{+0.13}_{-0.24}$	$1.514^{+0.000}_{-0.133}$	–	–	–
...	1.680 ± 0.006	–	$0.63^{+0.13}_{-0.24}$	...	–	–	–
SMC-126.1–00210	1.674 ± 0.037	−0.86 ± 0.15	$0.57^{+0.11}_{-0.13}$	$1.380^{+0.133}_{-0.092}$	–	–	–
...	1.669 ± 0.039	...	$0.58^{+0.08}_{-0.21}$	...	–	–	–
HD187669	1.505 ± 0.004	−0.25 ± 0.10	$0.31^{+0.18}_{-0.31}$	$2.455^{+0.057}_{-0.164}$	–	–	–
...	1.504 ± 0.004	...	$0.65^{+0.02}_{-0.45}$	...	–	–	–
OGLE-LMC-ECL-15260	1.426 ± 0.022	−0.47 ± 0.15	$0.00^{+0.50}_{-0.00}$	$2.291^{+0.164}_{-0.103}$	–	–	–
...	1.440 ± 0.024	...	$0.74^{+0.04}_{-0.46}$	...	–	–	–
AIPhe	1.234 ± 0.005	−0.14 ± 0.10	$0.39^{+0.03}_{-0.39}$	$4.677^{+0.2204}_{-0.2106}$	–	–	–
...	1.193 ± 0.004	...	$0.17^{+0.43}_{-0.17}$	...	–	–	–
YZCas	2.263 ± 0.012	0.01 ± 0.11	$0.80^{+0.00}_{-0.24}$	$0.575^{+0.000}_{-0.038}$	–	–	–
...	1.325 ± 0.007	...	$0.16^{+0.19}_{-0.16}$	...	–	–	–
TZFor	2.057 ± 0.001	0.01 ± 0.04	$0.46^{+0.07}_{-0.00}$	$1.230^{+0.000}_{-0.055}$	$0.75^{+0.04}_{-0.11}$	$1.097^{+0.026}_{-0.025}$	12
...	1.958 ± 0.001	...	$0.55^{+0.10}_{-0.06}$	...	$0.40^{+0.01}_{-0.25}$	...	...
V442Cyg	1.560 ± 0.024	–	$0.80^{+0.00}_{-0.41}$	$1.738^{+0.041}_{-0.189}$	–	–	–
...	1.407 ± 0.023	–	$0.10^{+0.42}_{-0.10}$	...	–	–	–
GXGem	1.488 ± 0.011	−0.12 ± 0.10	$0.45^{+0.15}_{-0.08}$	$2.630^{+0.000}_{-0.339}$	–	–	–
...	1.467 ± 0.010	...	$0.40^{+0.13}_{-0.07}$	...	–	–	–
BWAqr	1.479 ± 0.019	−0.07 ± 0.11	$0.44^{+0.09}_{-0.30}$	$2.455^{+0.176}_{-0.111}$	–	–	–
...	1.377 ± 0.021	...	$0.04^{+0.33}_{-0.04}$	...	–	–	–
AQSer	1.417 ± 0.021	–	$0.80^{+0.00}_{-0.26}$	$2.884^{+0.067}_{-0.254}$	–	–	–
...	1.346 ± 0.024	–	$0.60^{+0.20}_{-0.37}$	...	–	–	–
BFDra	1.414 ± 0.003	−0.03 ± 0.15	$0.66^{+0.09}_{-0.28}$	$2.818^{+0.202}_{-0.127}$	–	–	–
...	1.375 ± 0.003	...	$0.50^{+0.11}_{-0.33}$	...	–	–	–
BKPeg	1.414 ± 0.007	−0.12 ± 0.07	$0.44^{+0.03}_{-0.24}$	$2.754^{+0.064}_{-0.124}$	–	–	–
...	1.257 ± 0.005	...	$0.00^{+0.30}_{-0.00}$	...	–	–	–
COAnd	1.2892 ± 0.0073	+0.01 ± 0.15	$0.47^{+0.19}_{-0.21}$	$3.981^{+0.000}_{-0.514}$	–	–	–
...	1.2643 ± 0.0073	...	$0.40^{+0.21}_{-0.21}$	...	–	–	–

properly weight all the models with stellar properties close to the observed ones, and to derive the PDFs and credible intervals for the model parameters.

In the first part of the analysis (Section 4) we consider the hypothesis that only overshooting is responsible for the extra mixing and we try to reproduce the observed data by varying the overshooting efficiency parameter, λ_{ov}, in the models. Because of the significant scatter and the error bars, we do not find a clear trend of the λ_{ov} parameter, but we may expect that it grows from zero to its full efficiency regime in the mass domain between 1 and $\sim$1.5 $M_\odot$ and, thereafter, it remains constant, up to about $M_i \sim 5\,M_\odot$. Furthermore, our analysis clearly shows that, above $M_i \sim 1.5\,M_\odot$, the overshooting parameter is generally confined between $\lambda_{ov} \geq 0.3$–0.4 and $\lambda_{ov} \leq 0.8$. Such a large scatter of the extra mixing is difficult to explain in the framework of the usually adopted models of convection, which instead predict a constant efficiency for a given mass. In other words, the result of our analysis would require an overshooting parameter with a large stochastic variation in the range of intermediate-mass stars. We infer, from the distribution of the λ_{ov} parameter as a function of the initial mass depicted in Fig. 5, that there may be a concurrence between overshooting that sets a constant minimum threshold extra mixing, and a further effect that adds extra mixing in a stochastic way. This could be obtained by changing other stellar parameters, such as the adopted mixing length parameter (Claret & Torres 2016, 2017, 2018), the helium content (Valle et al. 2017), and even the inclusion of some mechanisms that may distort the observed luminosities and effective temperatures, like stellar spots (see e.g. Higl & Weiss 2017).

We suggest, instead, that rotation provides a more reasonable explanation for this stochastic extra mixing. In the second part of the analysis, we explore this hypothesis with models with a fixed overshooting parameter and at varying initial rotation rates. Our results, shown in Fig. 9, indicate that initial rotation rates in the interval $0 \leq \omega \leq 0.8$, combined with a mild overshooting distance of $\lambda_{ov} = 0.4$, may easily reproduce all the observed data above $M_i \sim 1.9\,M_\odot$. We stress that most of our stars in this mass range are now observed in an evolved phase and as slow rotators; thus, they are not affected by other effects such as gravity darkening.

We can also check if rotation is the only agent of extra mixing. To this purpose, we compute sets of models with no overshooting and a variable rotation rate. The right-hand panel of Fig. 11 shows a comparison between tracks with a mild overshooting ($\lambda_{ov} = 0.4$) and without rotation, and tracks with no overshooting and with rotation ($\omega = 0.6$). We note that, irrespective of the mixing scheme adopted, models with initial mass between 2.8 and 5.0 $M_\odot$ cross the Hertzsprung gap at the same luminosity, indicating a similar global

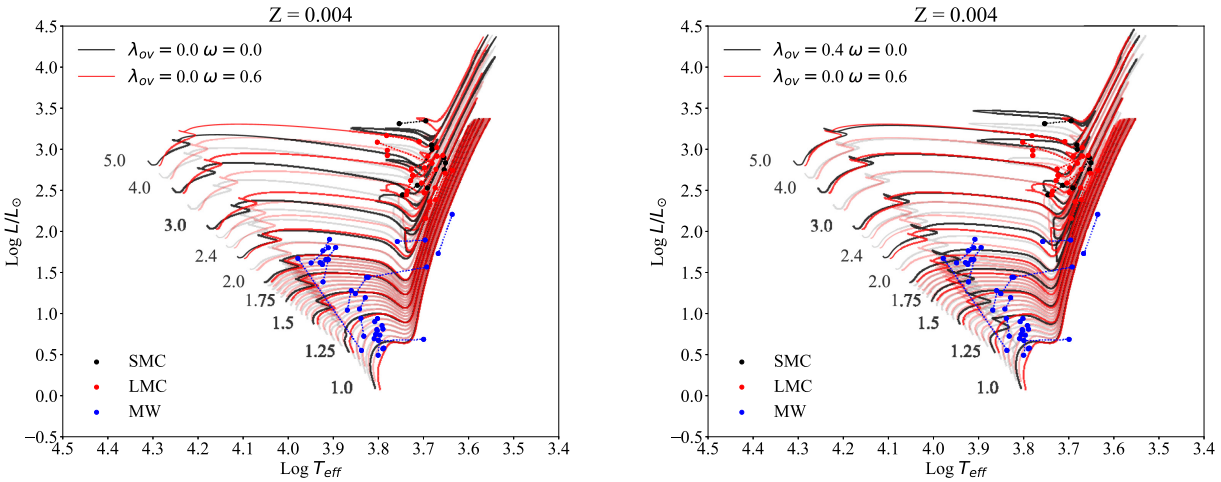

Figure 11. Same as Fig. 7, but on the left are tracks with fixed $\lambda_{ov} = 0.0$ and without rotation (in black), and with rotation of $\omega = 0.6$ (red lines), and on the right are tracks with $\lambda_{ov} = 0.4$ without rotation (in black), and tracks with $\lambda_{ov} = 0.0$ and rotation, with $\omega = 0.6$, in red. All the sets of tracks cover the mass range from 1 to 5 $M_{\odot}$, with $Z = 0.004$.

mixing during the main sequence. Thus, in order to reproduce a minimum extra mixing corresponding to $\lambda_{ov} = 0.4$, the threshold value in Fig. 5, *all* objects with initial mass $M_i \geq 1.9\,M_{\odot}$ should have been fast rotators in the early main sequence, with at least $\omega \geq 0.6$. While such a possibility cannot be excluded for binary stars, we recall that most of our components reside in detached systems (Claret & Torres 2016). Thus, this possibility is unlikely given that many single stars in this mass range are observed to possess small initial rotational velocities (Goudfrooij et al. 2018).

We conclude our discussion by considering in more detail the case of α Aurigae and TZ Fornacis, two of the best-studied objects in our sample. Observed quantities of individual components (Torres et al. 2015; Gallenne et al. 2016), in particular rotational velocities, can be compared to the predictions of our analysis. To this purpose, we compute evolutionary tracks with initial parameters appropriated for the binary components that result from the analysis performed with fixed overshooting and variable rotation. The comparisons with α Aurigae and TZ Fornacis are shown in Fig. 12. All the models are computed with $\lambda_{ov} = 0.4$. As far as the initial rotational velocities are concerned, we adopt $\omega_{\alpha A1} = 0.68$ for the primary star of α Aurigae and $\omega_{\alpha A2} = 0.73$ for the secondary, while for TZ Fornacis we adopt $\omega_{TZ1} = 0.75$ and $\omega_{TZ2} = 0.40$ for the primary and secondary, respectively (Table 5). We note that, since we are dealing with evolved stars, fully accounting for geometrical distortions will not significantly affect our results. Indeed, the adopted initial values of ω imply values smaller than 0.5 for the present secondary of α Aurigae, which translate into deviations from sphericity, $1 - R_{eq}/R_{pol}$, smaller than 4 per cent, and a maximum temperature excursion of 240 K from the equator to the pole. For TZ Fornacis the secondary has a present $\omega = 0.32$, which implies $1 - R_{eq}/R_{pol} = 1.5$ per cent and 100 K of T_{eff} excursion. Other stars in the $M_i > 1.9\,M_{\odot}$ sample present even smaller deviations since they correspond to more evolved stars. A more detailed investigation of individual objects with high rotational rates, including less evolved stars with $M_i < 1.9\,M_{\odot}$, should take into account geometric distortion and gravity-darkening effects, and will be pursued in a forthcoming work (Costa et al., in preparation).

The top panels in Fig. 12 show the evolution of the stellar radius, plotted as a function of the effective temperature. For the primary component of α Aurigae, it is difficult to distinguish whether the star is on the ascent of the red giant branch or in the helium-burning phase. However, inspection of the evolutionary track together with the uncertainties in the best-fitting parameters indicates that the star is in the helium-burning phase. The plots also indicate that its companion is at the end of the Hertzsprung gap. As for the TZ Fornacis system, we find that the primary component is in the He-burning phase, while the secondary, for the adopted best-fitting value of ω and accounting for the uncertainties in the radius, effective temperature, and age, turns out to be just at the beginning of the post-MS. In the bottom panels, we show the comparison between the tangential velocities of the models and the observed values of the projected velocity. Given that the latter values constitute only lower limits to the real equatorial velocities, we see that our analysis provides initial rotational velocities in good agreement with the observations.

Of particular interest are the secondary components of the two systems because they are in the subgiant phase, and still keep memory of the initial rotation rate. Our best fit of α Aurigae predicts a current equatorial velocity of $V_{eq}(\alpha A_2) \sim 66\,km\,s^{-1}$ while the observed value is $V \sin i\,(\alpha A_2) = 35\,km\,s^{-1}$. At face value it implies an inclination angle of the star pole with respect to the line of sight of $i \sim 32^{\circ}$. Our models with rotation indicate that in order to to obtain $V_{eq}(\alpha A_2) > 40\,km\,s^{-1}$ an initial rotation rate of $\omega > 0.5$ should have been necessary. The result of our analysis, based only on spectrophotometric properties of the components without any prior information on the rotational velocity, and suggesting that the secondary component of α Aurigae was a fast rotator with $\omega \sim 0.73$, is thus reinforced by the independent observation of its current rotational velocity. For the secondary component of TZ Fornacis, the best fit predicts a current equatorial velocity of $V_{eq}(TZF_2) \sim 53\,km\,s^{-1}$. The observed value is $V \sin i\ (TZF_2) = 46\,km\,s^{-1}$, implying an inclination angle $i \sim 60^{\circ}$. Thus, the secondary star of TZ Fornacis also provides direct independent evidence that the initial rotation rate of the secondary

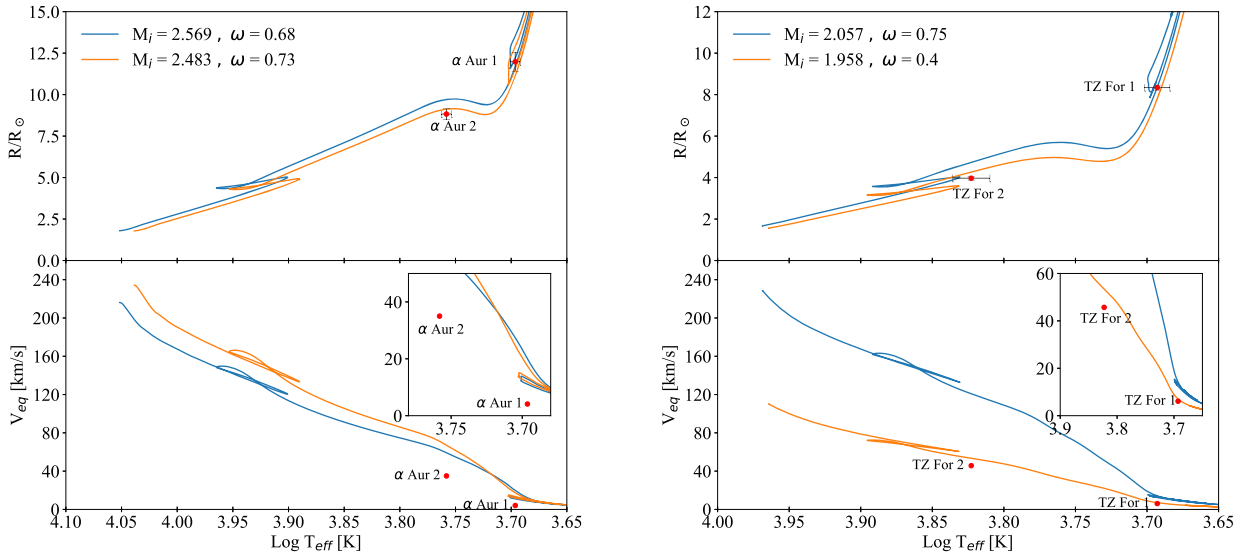

Figure 12. Comparison between the observed quantities (red points) and evolutionary tracks (continuous lines) for the α Aurigae (left-hand panels) and TZ Fornacis (right-hand panels) systems. The top panels plot the radius versus the logarithm of $T_{\rm eff}$. The bottom panels present the equatorial tangential velocities of the stars versus $T_{\rm eff}$. Blue and orange lines are the tracks aimed at representing the primary and secondary components, respectively.

component was not negligible (see also Higl et al. 2018), even if not as high as that of α Aur$_2$.

It is worth noticing that the predicted current equatorial velocity for TZ For$_2$ is near the minimum of its possible value. Using an overshooting distance significantly larger than $\lambda_{\rm ov} = 0.4$ would result in a lower initial ω, thus producing a tension with the current observed value. This is already suggested by the plot in Fig. 5. Thus, the test of TZ For$_2$ strongly supports our independent finding that the threshold efficiency of the overshooting process is $\lambda_{\rm ov} \sim 0.4$.

Finally, we can conclude that our study provides an insight into the extra mixing processes in stars, and gives strong suggestions that there is a concurrence between the overshooting effect and rotation in low–intermediate-mass stars.

In summary we conclude that the spectrophotometric properties of detached double-lined eclipsing binaries are well reproduced by assuming a threshold core overshooting distance, in the Bressan et al. (1981) scheme, of $\lambda_{\rm ov} \sim 0.4$ with an additional effect of rotation that, by its nature, introduces a significant star-to-star variation of the global mixing.

ACKNOWLEDGEMENTS

GC thanks Giovanni Mirouh for the fruitful discussions on stellar rotation. We acknowledge the support from the ERC Consolidator Grant funding scheme (*project STARKEY*, G.A. n. 615604). TSR acknowledges financial support from Premiale 2015 MITiC (PI B. Garilli). For the plots we used MATPLOTLIB, a PYTHON library for publication quality graphics (Hunter 2007).

REFERENCES

Arnett W. D., Meakin C., Hirschi R., Cristini A., Georgy C., Campbell S., Scott L. J. A., Kaiser E. A., 2018, preprint (arXiv:1810.04659)
Bertelli G., Girardi L., Marigo P., Nasi E., 2008, A&A, 484, 815
Böhm-Vitense E., 1958, Z. Astrophys., 46, 108
Bossini D. et al., 2017, MNRAS, 469, 4718
Brandt T. D., Huang C. X., 2015, ApJ, 807, 25
Bressan A. G., Chiosi C., Bertelli G., 1981, A&A, 102, 25
Bressan A., Bertelli G., Chiosi C., 1986, Mem. Soc. Astron. Ital., 57, 411
Bressan A., Marigo P., Girardi L., Salasnich B., Dal Cero C., Rubele S., Nanni A., 2012, MNRAS, 427, 127
Brott I. et al., 2011a, A&A, 530, A115
Brott I. et al., 2011b, A&A, 530, A116
Caffau E., Ludwig H.-G., Steffen M., Freytag B., Bonifacio P., 2011, Sol. Phys., 268, 255
Chen Y., Girardi L., Bressan A., Marigo P., Barbieri M., Kong X., 2014, MNRAS, 444, 2525
Chen Y., Bressan A., Girardi L., Marigo P., Kong X., Lanza A., 2015, MNRAS, 452, 1068
Chieffi A., Limongi M., 2013, ApJ, 764, 21
Chieffi A., Limongi M., 2017, ApJ, 836, 79
Choi J., Dotter A., Conroy C., Cantiello M., Paxton B., Johnson B. D., 2016, ApJ, 823, 102
Claret A., Torres G., 2016, A&A, 592, A15
Claret A., Torres G., 2017, ApJ, 849, 18
Claret A., Torres G., 2018, ApJ, 859, 100
Constantino T., Baraffe I., 2018, A&A, 618, A177
da Silva L. et al., 2006, A&A, 458, 609
Demarque P., Woo J.-H., Kim Y.-C., Yi S. K., 2004, ApJS, 155, 667
Eggenberger P., Meynet G., Maeder A., Hirschi R., Charbonnel C., Talon S., Ekström S., 2008, Ap&SS, 316, 43
Ekström S. et al., 2012, A&A, 537, A146
Endal A. S., Sofia S., 1976, ApJ, 210, 184
Freytag B., Ludwig H.-G., Steffen M., 1996, A&A, 313, 497
Fu X., Bressan A., Marigo P., Girardi L., Montalban J., Chen Y., Nanni A., 2018, MNRAS, 16, 1
Gallenne A. et al., 2016, A&A, 586, A35
Goudfrooij P., Girardi L., Bellini A., Bressan A., Correnti M., Costa G., 2018, ApJ, 864, L3
Heger A., Langer N., 2000, ApJ, 544, 1016
Heger A., Langer N., Woosley S. E., 2000, ApJ, 528, 368
Hidalgo S. L. et al., 2018, ApJ, 856, 125
Higl J., Weiss A., 2017, A&A, 608, A62
Higl J., Siess L., Weiss A., Ritter H., 2018, A&A, 617, A36
Hunter J. D., 2007, Comput. Sci. Eng., 9, 90
Keller S. C., Wood P. R., 2006, ApJ, 642, 834
Kippenhahn R., Thomas H., 1970, Stellar Rotation, Proc. IAU Colloq. 4. Gordon and Breach Science Publishers, London, p. 20

Kippenhahn R., Weigert A., Weiss A., 2012, Stellar Structure and Evolution, 2nd edn. Springer, Heidelberg
Kroupa P., 2002, Science, 295, 82
Maeder A., 1975, A&A, 40, 303
Maeder A., 2009, Physics, Formation and Evolution of Rotating Stars. Springer, Heidelberg
Maeder A., Zahn J.-P., 1998, A&A, 1006, 1000
Maeder A., Meynet G., Lagarde N., Charbonnel C., 2013, A&A, 553, A1
Magic Z., Weiss A., Asplund M., 2015, A&A, 573, A89
Marino A. F., Przybilla N., Milone A. P., Da Costa G., D'Antona F., Dotter A., Dupree A., 2018a, AJ, 156, 116
Marino A. F., Milone A. P., Casagrande L., Przybilla N., Balaguer-Nú nez L., Di Criscienzo M., Serenelli A., Vilardell F., 2018b, ApJ, 863, L33
Meynet G., Maeder A., 1997, A&A, 321, 465
Moravveji E., Aerts C., Pápics P. I., Triana S. A., Vandoren B., 2015, A&A, 580, A27
Mowlavi N., Eggenberger P., Meynet G., Ekström S., Georgy C., Maeder A., Charbonnel C., Eyer L., 2012, A&A, 541, A41
Paxton B., Bildsten L., Dotter A., Herwig F., Lesaffre P., Timmes F., 2011, ApJS, 192, 3
Paxton B. et al., 2013, ApJS, 208, 4
Paxton B. et al., 2015, ApJS, 220, 15
Paxton B. et al., 2018, ApJS, 234, 34
Petrovic J., Langer N., Yoon S.-C., Heger A., 2005, A&A, 435, 247
Pietrinferni A., Cassisi S., Salaris M., Castelli F., 2004, ApJ, 612, 168
Potter A. T., Tout C. A., Eldridge J. J., 2012, MNRAS, 419, 748
Rodrigues T. S. et al., 2014, MNRAS, 445, 2758
Rodrigues T. S. et al., 2017, MNRAS, 467, 1433
Rosenfield P. et al., 2017, ApJ, 841, 69
Schwarzschild M., 1958, Structure and Evolution of the Stars.. Princeton, Princeton Univ. Press
Spada F., Demarque P., Kim Y.-C., Boyajian T. S., Brewer J. M., 2017, ApJ, 838, 161
Stancliffe R. J., Fossati L., Passy J.-C., Schneider F. R. N., 2015, A&A, 575, A117
Stancliffe R. J., Fossati L., Passy J.-C., Schneider F. R. N., 2016, A&A, 586, A119
Talon S., Zahn J.-P., 1997, A&A, 317, 749
Tang J., Bressan A., Rosenfield P., Slemer A., Marigo P., Girardi L., Bianchi L., 2014, MNRAS, 445, 4287
Torres G., Andersen J., Giménez A., 2010, A&AR, 18, 67
Torres G., Claret A., Pavlovski K., Dotter A., 2015, ApJ, 807, 26
Valle G., Dell'Omodarme M., Prada Moroni P. G., Degl'Innocenti S., 2016, A&A, 587, A16
Valle G., Dell'Omodarme M., Prada Moroni P. G., Degl'Innocenti S., 2017, A&A, 600, A41
Weiss A., Schlattl H., 2008, Ap&SS, 316, 99
Woo J.-H., Gallart C., Demarque P., Yi S., Zoccali M., 2003, AJ, 125, 754
Yoon S.-C., Langer N., 2005, A&A, 443, 643
Zahn J.-P., 1992, A&A, 265, 115

This paper has been typeset from a TEX/LATEX file prepared by the author.